

Contents

1	Introduction to Gravitational Waves	1
1.1	Mathematical Framework of Gravitational Waves	1
1.1.1	General Relativity Primer	2
1.1.2	Deriving Gravitational Waves from General Relativity	5
1.2	Gravitational Wave Sources	7
1.3	Gravitational Wave Data Analysis Techniques	10
1.3.1	Matched Filtering	10
1.3.2	Parameter Estimation	10
1.4	Introduction	11
1.5	Primordial Black Hole Formation Mechanisms	11
1.5.1	Inflationary Scenarios	12
1.5.2	Non-Inflationary Scenarios	15
1.5.3	Formation of PBH Binaries in the Present Universe	16
1.6	Primordial Black Holes and Gravitational Waves	17
1.6.1	Merger Event Rate of PBHs	18
1.6.2	Abundance of PBHs	20
1.6.3	Observational Constraints on Non-Evaporating PBHs	21
1.7	Primordial Black Holes as Dark Matter	25
2	PART I: Improving Sub-Solar Mass Searches for Primordial Black Holes	26
2.1	Introduction	27
2.1.1	GstLAL Search Pipeline	28
2.1.2	Singular Value Decomposition (SVD)	28
2.2	Random Projection-Based Singular Value Decomposition (RSVD)	31
2.2.1	Random Projections (RP)	31
2.2.2	Generating a Random Matrix	34
2.2.3	Randomized-SVD	34
2.2.4	Summary Page of RSVD	35
2.2.5	What do we do with the B matrix?	37
2.2.6	SNR Reconstruction	37
2.3	Comparison between SVD and RSVD	39
2.4	Discussion and Conclusion	43

3	PART II: Distinguishing Primordial Black Holes from Astrophysical Black Holes in the Lower Mass Gap Region	45
3.1	Introduction	46
3.1.1	Studying the Lower Mass Gap Region	46
3.2	Parameter Estimation Primer	49
3.2.1	BILBY: The Tool	50
3.3	Methodology	52
3.3.1	Model Selection	52
3.3.2	Mock Populations and Injections	54
3.3.3	Parameter Estimation Techniques	55
3.4	Results and Discussion	61
3.5	Future Projects	66
3.5.1	Addition of Models	66
3.5.2	Differentiating between ABBH, PBBH and BNS Mergers	69
3.5.3	Case Studies of GW190425 and GW190814	71
3.5.4	Extending to the Upper Mass Gap Region	71

66section*.49

INTRODUCTION TO GRAVITATIONAL WAVES

In 1915, Albert Einstein published the theory of general relativity (GR) [1] which predicted that gravity can be described as an interaction between the geometry of spacetime and its matter-energy content. This dynamical relationship is expressed through the Einstein Field Equations:

$$G_{\alpha\beta} = 8\pi T_{\alpha\beta} \quad (1.1)$$

Originally, Henri Poincaré proposed the concept of gravitational waves in 1905. After publishing his theory, Einstein was skeptical about their existence but he pursued the concept. He finally predicted the existence of gravitational waves but he was also convinced that they could never be detected. Exactly a hundred years later, in 2015, the Laser Interferometer Gravitational-Wave Observatory (LIGO) detected gravitational waves for the first time using their detectors at Hanford and Livingston in USA. The discovery of gravitational waves has led to the emergence of a contemporary field in astronomy and astrophysics. In this chapter, I will first provide an intuitive understanding about gravitational waves and then proceed to provide the mathematical framework by bringing in general relativity.

1.1 Mathematical Framework of Gravitational Waves

Gravitational Waves (GWs) arise from General Relativity (GR). GR provides the mathematical framework to discuss the production and propagation of GWs through spacetime. In order to derive GWs from GR, it would be helpful to go over certain key aspects of GR that will help us understand the derivation better. Section 1.1.1 consists of a GR primer, you may skip it if

you are already familiar with the topic and move ahead to section 1.1.2 in which I derive GWs from GR.

1.1.1 General Relativity Primer

The final equations that GR provides us with are the Einstein Field Equations - a set of ten partial differential equations. These set of equations relate the curvature of spacetime to the mass and energy causing it. Essentially, this expression describes how matter tells spacetime to curve and how spacetime tells matter to move.

$$R_{\mu\nu} - \frac{1}{2}Rg_{\mu\nu} + \Lambda g_{\mu\nu} = 8\pi T_{\mu\nu} \quad (1.2)$$

The left hand side of this expression describes the curvature of spacetime. $R_{\mu\nu}$ is the Ricci tensor and R is the Ricci scalar, both contractions of the Riemann curvature tensor. Λ is the cosmological constant which represents the energy density of the vacuum of space. On the right hand side, $T_{\mu\nu}$ is the energy-momentum tensor that describes what is causing the curvature in spacetime. To understand this equation and the subsequent derivation better, let us look at each term in more detail.

We use the following conventions throughout this chapter:

1. **Natural Units:** $\hbar = c = G = 1$;
2. **Metric Sign Convention:** $g_{\mu\nu} = \text{diag}(-1, +1, +1, +1)$
3. **Einstein Summation Convention:** $a_i b^i = a_1 b^1 + a_2 b^2 + a_3 b^3 + a_4 b^4$ for the four dimensions;
4. **Notation for Partial Derivatives:** $\frac{\partial}{\partial \mu} \equiv \partial_\mu$

Metric Tensor $g_{\mu\nu}$

The metric is the most fundamental object in GR. In a way, this is the object that contains all the information about the geometry of spacetime and also helps us understand the relation between the local and global coordinates of a manifold. It can also be understood by considering the example of a contour map: a straight line of (say) 5 cm drawn on a 2-dimensional contour map does not provide us with a lot of information about what is happening *locally* i.e. we get no information about the nature of the contours. This is because the straight line we

are drawing is based on a different coordinate system than the contour map itself. In this case, the straight line is based on the 2-dimensional x-y coordinate system or the *global* coordinate system. To get a better idea of what is actually happening, we need a relation between the local coordinates and the global coordinates and this is where the metric tensor comes into play.

The metric essentially encodes the information about how to measure (spatial and temporal) distances via the associated line element. For example, the line element for standard 3-D Euclidean geometry is given by

$$ds^2 = dx^2 + dy^2 + dz^2, \quad (1.3)$$

and for flat Minkowski space, we have

$$ds^2 = -dt^2 + dx^2 + dy^2 + dz^2 \quad (1.4)$$

This can be rewritten using the Einstein Summation Convention and generalized as

$$\boxed{ds^2 = g_{\mu\nu}(x)dx^\mu dx^\nu}. \quad (1.5)$$

Christoffel Symbol $\Gamma_{\mu\nu}^\beta$

The Christoffel symbol arises when a vector is parallel-transported on a curved manifold¹. If we look at transporting a vector in flat space, we consider the Laplacian of a scalar in three flat dimensions (x, y, z) :

$$\nabla^a \nabla_a \phi = \frac{\partial^2 \phi}{\partial x^2} + \frac{\partial^2 \phi}{\partial y^2} + \frac{\partial^2 \phi}{\partial z^2}. \quad (1.6)$$

However, if we consider cylindrical coordinates (r, θ, z) instead, the Laplacian becomes

$$\nabla^a \nabla_a \phi = \frac{\partial^2 \phi}{\partial r^2} + \frac{1}{r^2} \left(\frac{\partial^2 \phi}{\partial \theta^2} \right) + \frac{\partial^2 \phi}{\partial z^2} - \frac{1}{r} \left(\frac{\partial \phi}{\partial r} \right), \quad (1.7)$$

where we have second derivatives of ϕ , similar to 1.6. But we also have **first** order derivatives of ϕ ; this is where the Christoffel symbols become relevant. A general expression for the Laplacian operator is given by

$$\nabla_a \nabla^a \phi = g^{ab} \partial_a \partial_b \phi - g^{ab} \Gamma_{ab}^c \partial_c \phi, \quad (1.8)$$

where Γ_{ab}^c is the Christoffel symbol. It helps to encode the difference between the local and global coordinates that arises when considering a curved manifold and hence, is essentially described by the metric:

$$\boxed{\Gamma_{\mu\nu}^\sigma = \frac{1}{2} g^{\sigma\rho} (\partial_\mu g_{\nu\rho} + \partial_\nu g_{\rho\mu} - \partial_\rho g_{\mu\nu})}. \quad (1.9)$$

¹A manifold is a possible curved space that in small enough regions, looks flat.

Riemann Curvature Tensor $R^\lambda_{\sigma\mu\nu}$

The nature of spacetime across the universe is curved if matter and energy is present. This leads us to consider curved manifolds and naturally, we cannot use Cartesian flat coordinates to describe them. Instead, we have the Riemann curvature tensor which encodes the curvature information using the metric tensor g_{ab} and the Christoffel symbols $\Gamma^\sigma_{\mu\nu}$. In short, this tensor can be used to conclusively determine whether a manifold is flat ($R^\lambda_{\sigma\mu\nu} = 0$) or curved. The Riemann curvature tensor is given by

$$R^\sigma_{\mu\alpha\beta} \equiv \partial_\alpha \Gamma^\sigma_{\mu\beta} - \partial_\beta \Gamma^\sigma_{\mu\alpha} + \Gamma^\sigma_{\alpha\lambda} \Gamma^\lambda_{\mu\beta} - \Gamma^\sigma_{\beta\lambda} \Gamma^\lambda_{\mu\alpha}. \quad (1.10)$$

Ricci Tensor $R_{\alpha\beta}$ and the Ricci Scalar R

There are two contractions of the Riemann curvature tensor that are extremely useful - the Ricci tensor $R_{\alpha\beta}$ and the Ricci Scalar R .

$$R_{\alpha\beta} = R^\lambda_{\alpha\lambda\beta}; \quad (1.11)$$

$$R = R^\lambda_\lambda = g^{\mu\nu} R_{\mu\nu}; \quad (1.12)$$

Using all the definitions above, we can finally define the **Einstein Tensor** as

$$G_{\mu\nu} \equiv R_{\mu\nu} - \frac{1}{2} R g_{\mu\nu}. \quad (1.13)$$

Energy-Momentum Tensor $T_{\mu\nu}$

For completeness of this section, it is important to also introduce the tensor which describes the density and flux of momentum and energy. This tensor encodes information about the content of matter of spacetime, "telling" it how to curve. For a perfect fluid, it is given by

$$T^{\mu\nu} \equiv \left(\rho + \frac{p}{c^2} \right) \frac{dx^\mu}{d\tau} \frac{dx^\nu}{d\tau} - p g^{\mu\nu}, \quad (1.14)$$

where ρ and p represent density and pressure respectively.

Einstein's Field Equations (EFE)

Finally, we have all the elements to write Einstein's field equations (EFE) that explains how the curvature of spacetime causes gravitational interaction.

$$\boxed{G^{\mu\nu} = -\frac{8\pi G}{c^4} T^{\mu\nu}} \quad (1.15)$$

1.1.2 Deriving Gravitational Waves from General Relativity

We consider the Minkowski metric for flat space $\eta_{\mu\nu} = \text{diag}(-1, 1, 1, 1)$ along with a small perturbation $h_{\mu\nu}$. $h_{\mu\nu}$ is a small and unknown perturbation on flat space. We use this metric to finally derive the linearized Einstein Field Equations and subsequently, gravitational waves. So the metric we will consider for the derivation can be written as

$$g_{\mu\nu} = \eta_{\mu\nu} + h_{\mu\nu} \text{ where } |h_{\mu\nu}| \ll 1, \quad (1.16)$$

which means that we drop terms which are quadratic or of higher power in $h_{\mu\nu}$. Using this metric, it is straightforward to compute the Christoffel symbols and the curvature tensors.

$$\partial_\rho g_{\mu\nu} = \partial_\rho \eta_{\mu\nu} + \partial_\rho h_{\mu\nu} = \partial_\rho h_{\mu\nu} \quad (1.17)$$

Substituting this expression into the expression for Christoffel symbols (1.9), we get:

$$\Gamma_{\mu\nu}^\rho = \frac{1}{2} \eta^{\rho\sigma} (\partial_\mu h_{\nu\sigma} + \partial_\nu h_{\mu\sigma} - \partial_\sigma h_{\mu\nu}) \quad (1.18)$$

where we have neglected the higher order $\mathcal{O}(h^2)$ terms. This might not seem like a fair approximation when we think of events involving compact objects and highly curved spacetime since the metric and the subsequent expressions can become very complicated with multiple higher-order terms. However, we are interested only in considering the metric of spacetime near the observer (for example, on earth) who is far away from the event itself. The GWs reaching this observer are expected to be very weak and hence, our approximation holds correct in this scenario.

Next, we calculate the Riemann curvature tensor:

$$\begin{aligned} R_{\mu\nu\rho\sigma} &= \eta_{\nu\tau} R_{\nu\rho\sigma}^\tau \\ &= \eta_{\nu\tau} (\partial_\rho \Gamma_{\nu\sigma}^\tau - \partial_\sigma \Gamma_{\nu\rho}^\tau). \end{aligned} \quad (1.19)$$

We have already calculated the Christoffel symbols so we can simply plug them into the above expression to get:

$$\begin{aligned}
 R_{\mu\nu\rho\sigma} &= \eta_{\nu\tau} \left\langle \partial_\rho \left[\frac{1}{2} \eta^{\tau\alpha} (\partial_\nu h_{\sigma\alpha} + \partial_\sigma h_{\nu\alpha} - \partial_\alpha h_{\nu\sigma}) \right] - \partial_\sigma \left[\frac{1}{2} \eta^{\tau\beta} (\partial_\nu h_{\rho\beta} + \partial_\rho h_{\nu\beta} - \partial_\beta h_{\nu\rho}) \right] \right\rangle \\
 &= \frac{1}{2} \partial_\rho [\eta_\mu^\alpha (\partial_\nu h_{\sigma\alpha} + \partial_\sigma h_{\nu\alpha} - \partial_\alpha h_{\nu\sigma})] - \frac{1}{2} \partial_\sigma [\eta_\mu^\beta (\partial_\nu h_{\rho\beta} + \partial_\rho h_{\nu\beta} - \partial_\beta h_{\nu\rho})] \\
 &= \frac{1}{2} \partial_\rho [\partial_\nu h_{\sigma\mu} + \partial_\sigma h_{\nu\mu} - \partial_\mu h_{\nu\sigma}] - \frac{1}{2} \partial_\sigma [\partial_\nu h_{\rho\mu} + \partial_\rho h_{\nu\mu} - \partial_\mu h_{\nu\rho}] \\
 &= \frac{1}{2} [\partial_\rho \partial_\nu h_{\sigma\mu} - \partial_\rho \partial_\mu h_{\nu\sigma} - \partial_\sigma \partial_\nu h_{\rho\mu} + \partial_\sigma \partial_\mu h_{\nu\rho}].
 \end{aligned} \tag{1.20}$$

The Ricci tensor, as discussed in the previous section, is a contraction of the Riemann curvature tensor:

$$\begin{aligned}
 R_{\nu\sigma} &= \eta^{\rho\mu} R_{\mu\nu\rho\sigma} \\
 &= \frac{1}{2} [\partial^\mu \partial_\nu h_{\sigma\mu} - \partial^\mu \partial_\mu h_{\nu\sigma} - \partial_\sigma \partial_\nu h + \partial_\sigma \partial_\mu h_\nu^\mu] \\
 &= \frac{1}{2} [\partial^\mu \partial_\nu h_{\sigma\mu} - \square h_{\nu\sigma} - \partial_\sigma \partial_\nu h + \partial_\sigma \partial^\mu h_{\nu\mu}],
 \end{aligned} \tag{1.21}$$

where we have used $\eta^{\alpha\beta} h_{\alpha\beta} = h$ and the definition of the d'Alembertian $\square = \partial_\mu \partial^\mu$.

To find the Ricci scalar, we need to contract the expression once more:

$$\begin{aligned}
 R &= \eta^{v\sigma} R_{\sigma v} \\
 &= \frac{1}{2} [\partial^\mu \partial_\nu h_\mu^\nu - \partial^\mu \partial_\mu h_{\nu\sigma} - \partial^\nu \partial_\nu h + \partial_\sigma \partial^\mu h_\mu^\sigma] \\
 &= \partial_\mu \partial_\nu h^{\mu\nu} - \square h
 \end{aligned} \tag{1.22}$$

We finally have all the elements required to obtain the Einstein Field Equations (1.15); we ignore the cosmological constant and continue to omit the higher order $\mathcal{O}(h^2)$ terms.

$$\begin{aligned}
 8\pi T_{\mu\nu} &= \frac{1}{2} [\partial^\alpha \partial_\mu h_{\nu\alpha} - \square h_{\mu\nu} - \partial_\mu \partial_\nu h + \partial_\nu \partial^\alpha h_{\mu\alpha}] - \frac{1}{2} \eta_{\mu\nu} [\partial_\mu \partial_\nu h^{\mu\nu} - \square h] \\
 16\pi T_{\mu\nu} &= \partial^\alpha \partial_\mu h_{\nu\alpha} - \square h_{\mu\nu} + \partial_\nu \partial^\alpha h_{\mu\alpha} - \eta_{\mu\nu} \partial_\mu \partial_\nu h^{\mu\nu},
 \end{aligned} \tag{1.23}$$

where $\eta_{\mu\nu} \square h = \partial_\nu \partial_\mu h$.

The above equation looks rather complicated - to simplify it further, we can choose appropriate *gauge conditions*. First, we need a coordinate system where the Lorenz gauge holds i.e.

$\partial^\mu \bar{h}_{\mu\nu} = 0$. Second, we define the trace-reversed perturbation $\bar{h}_{\mu\nu} = h_{\mu\nu} - \frac{h}{2}\eta_{\mu\nu}$ in this coordinate system such that the trace of \bar{h} is $\bar{h} = \bar{h}^\mu_\mu = -h$. Using the trace-reversed perturbation expressions, Eqn. 1.23 becomes

$$16\pi T_{\mu\nu} = \partial^\alpha \partial_\mu \bar{h}_{\nu\alpha} - \square \bar{h}_{\mu\nu} + \partial_\nu \partial^\alpha \bar{h}_{\mu\alpha} - \eta_{\mu\nu} \partial_\mu \partial_\nu \bar{h}^{\mu\nu}, \quad (1.24)$$

since $\partial_\rho \frac{h}{2} \eta_{\mu\nu} = 0$.

Finally, our simplified linearized EFE expression becomes:

$$16\pi T_{\mu\nu} = -\square \bar{h}_{\mu\nu}. \quad (1.25)$$

Since our observer is far away from the source, the stress-energy tensor $T_{\mu\nu}$ vanishes. This reduces the EFE expression further to a straightforward wave equation:

$$\square \bar{h}_{\mu\nu} \equiv \left(-\frac{1}{c^2} \partial_t^2 + \nabla^2\right) \bar{h}_{\mu\nu} = 0 \quad (1.26)$$

The solution to this wave equation is a simple plane wave

$$\bar{h}_{\mu\nu}(t) = A_{\mu\nu} \cos(\omega t - \mathbf{k} \cdot \mathbf{x}). \quad (1.27)$$

A conclusion to this derivation, in simple words, is that gravitational waves cause ripples in spacetime that spread widely. Hence, they can also be detected far from the source.

1.2 Gravitational Wave Sources

In principle, every non-symmetric and accelerating event in the universe produces gravitational waves. For example, a perfectly spherical and spinning star would not produce GWs but a slightly asymmetric star would. However, the present-day GW detectors are not sensitive enough to detect all the GWs in the universe. As of now, they are equivalent to the audible frequency range if GWs were sound waves. There are many astrophysical sources of GWs but broadly, they are divided into four categories - continuous, inspiral, burst and stochastic. (Fig. 1.1)

1. **Continuous Sources:** Continuous GWs are produced from sources with constant and well-defined values of frequency. A single spinning star with a small bump on its surface would produce continuous GWs, for example.
2. **Inspiral Sources:** The main inspiral GW sources are Compact Binary Coalescences (CBCs). As the name suggests - these are events of two compact binary objects spiraling

around each and finally coalescing to form a single merger. Inspiral GWs naturally correspond to the inspiral phase of such an event. Binary black holes and binary neutron stars are the main CBC events and are of great interest with regard to the detections that are made by the LVC detectors.

3. **Burst Sources:** Burst sources are possibly the most mysterious of all events. These are usually small bumps seen in the spectrum, as shown in the example signal. The sources of these bumps are unknown and they do not come from any anticipated events.
4. **Stochastic Sources:** Stochastic GWs are equivalent to the background noise of the cosmos, relics of the GWs from the early universe. These waves are very interesting as they possibly contain information about the Big Bang and the early universe.

In this thesis, we are concerned with the GWs that are produced by merging primordial binary black holes (PBBHs). In Chapter 2, we discuss the origin of PBBHs in extensive detail and discover that broadly, PBBHs fall under the categories of both inspiral and stochastic sources of GWs.

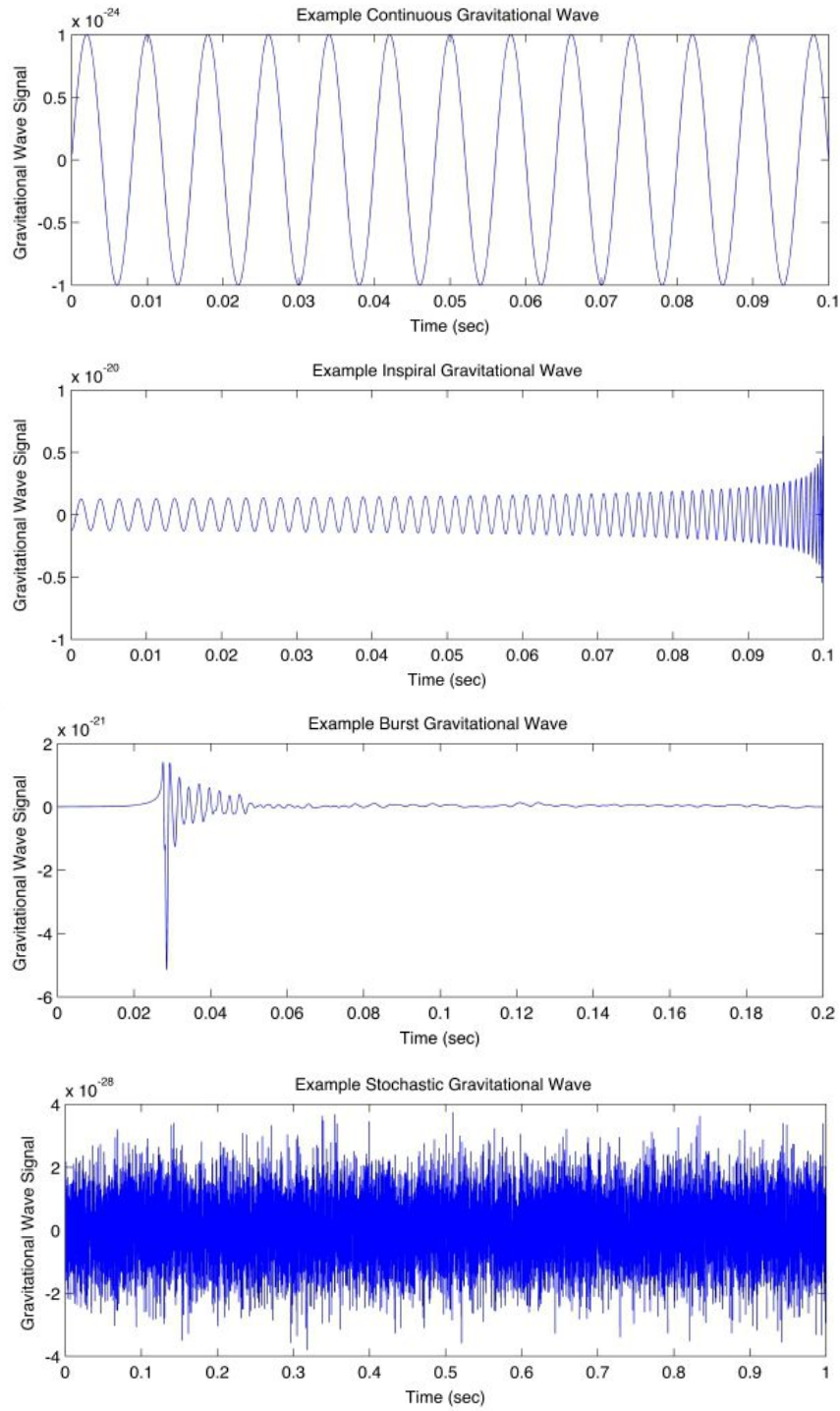


Figure 1.1: **Gravitational Wave Sources** (A. Stuver/LIGO)

1.3 Gravitational Wave Data Analysis Techniques

1.3.1 Matched Filtering

One of the most important data analysis techniques used for detecting GWs is matched filtering. This technique is used to see if our data has any hidden GW signals. The final aim of matched filtering is to compare these hidden signals with known templates and confirm a GW detection.

Numerical relativity techniques are used to run simulations that generate templates of various GW waveforms for a range of different merging systems. Finally, all these templates are added to template banks which are used for further analysis. A 'match' between a signal in the detector data and one of these generated templates would lead to a confident detection as seen in Fig. 1.2. There are two main matched filtering search pipelines that are used within the LVC collaboration currently - GstLAL and PyCBC. Matched filtering uses a lot of computational power, as I'll discuss in a later chapter (2.2). This makes it very important to choose the template bank wisely.

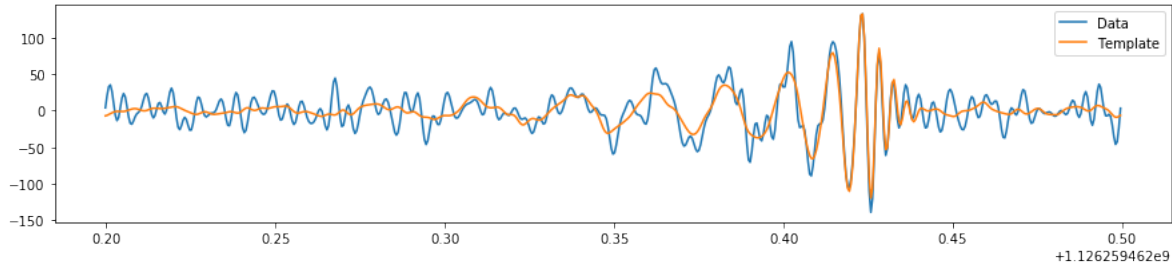


Figure 1.2: **Matched Filtering**: visualizing the overlap between the template and data using PyCBC

1.3.2 Parameter Estimation

Bayesian analysis and parameter estimation together form the language of GW astronomy [2]. After a detection, these techniques make it possible to derive various source properties including sky locations, component masses, spin properties, and other parameters. For the first ever GW detection (GW150914), the black hole masses were determined to be $35^{+5}_{-3}M_{\odot}$ and $33^{+3}_{-4}M_{\odot}$ [3]. These techniques were also used to help determine that the event GW170104 took place 880^{+450}_{-390} Mpc away from earth. In Part II of this thesis, I use parameter estimation extensively. A brief primer to it can be referred to in 3.2.

1.4 Introduction

Massive stars in our Universe are born, go through various stages of stellar evolution for millions of years and finally die to produce a black hole. These black holes are called stellar black holes or astrophysical black holes. However, theories predict that there are black holes that exist in the early Universe. These black holes are thought to have come into existence soon after inflation during the radiation-dominated era, approximately 47,000 years after the Big Bang. Naturally, there was not enough time for stars to be born, live their entire lives and die to form black holes in such a short period of time. So what are these objects and how did they form?

Primordial Black Holes (PBHs) are theorized objects that formed in the early Universe as a result of the great compression associated with the Big Bang and exist over all mass ranges. [4] They are extremely interesting objects to study, although little is known about them. These objects could hold answers to many key questions of early-Universe cosmology and are also considered as good candidates for dark matter.

Zeldovich and Novikov first pointed out in 1967 that black holes in the early Universe may grow by accreting the surrounding radiation. [5] This was further theorized by Hawking in 1971 [6] when he suggested that a large number of gravitationally collapsed objects of masses as low as 10^{-5} g were formed as a result of fluctuations in the early Universe. This led to the earliest theory of PBH formation. Once inflationary cosmology grew more important, the formation of PBHs and their properties have been studied in direct relation to the inflation models of the Universe. But conversely, the observation of PBHs would greatly contribute to building these models which ultimately would help understand the early Universe better. While detecting a primordial black hole would be a huge scientific breakthrough, it is also important to mention that even a confident non-detection would be beneficial to inflationary cosmology models and dark matter studies.

1.5 Primordial Black Hole Formation Mechanisms

A plethora of formation mechanism theories have been developed, in an attempt to understand primordial black holes better. Very broadly, PBH formation mechanism theories are of two types - inflationary and non-inflationary scenarios. Both scenarios begin with density inhomogeneities in certain regions of the Universe that lead to a gravitational collapse giving rise to a PBH. The main difference lies in the theory of how these inhomogeneities come into existence.

1.5.1 Inflationary Scenarios

Inflation refers to the accelerated expansion in the early Universe. This acceleration is what drives the Universe to reach a state of homogeneity, isotropy and spatial flatness. About 10^{-32} seconds after the inflation era or 47,000 years after the Big Bang, the radiation-dominated era of the Universe began. PBHs formed in this era when a perturbed region entered the Hubble radius if the amplitude of the fluctuation exceeded the critical value $w \sim 1/3$. [7] It has also been concluded that the resultant PBH has a mass of order of the horizon mass at formation.

When two PBHs came closer, the surrounding PBHs and especially the closest one exerted torques on the bound system. This prevented the head-on collision of the two PBHs. They formed an eccentric binary instead. (Fig. 1.3)

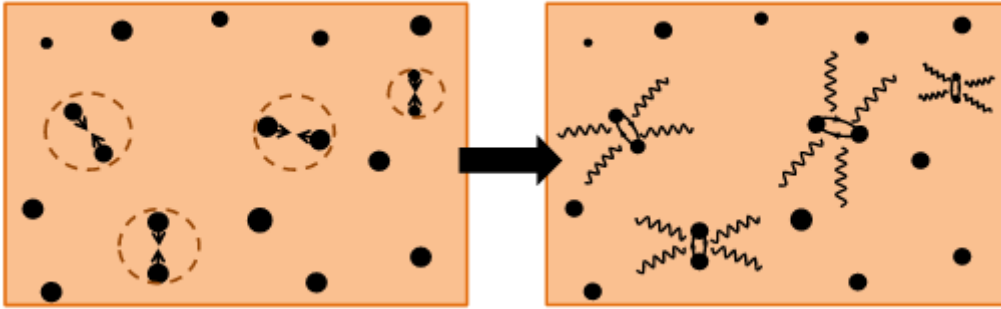


Figure 1.3: **Schematic representation of the formation of PBH binaries in the radiation-dominated Universe;** [8]

Mathematical Framework: Condition for PBH Formation in the Early Universe

In the early radiation-dominated Universe, a highly over-dense region would gravitationally collapse into a primordial black hole. Here, let us briefly review a rough sketch of PBH formation in the inflationary scenario. [8] It is important to note that this only provides us with an idea of the physics behind the formation of PBHs in the early Universe. However, it is not the most accurate version since there are many approximations and conditions that I have chosen to omit for the purpose of this thesis.

The background spacetime of the Universe after inflation can be well-described by the spatially-flat Friedmann-Lemaître-Robertson-Walker (FLRW) metric that describes homogeneous and

isotropic space:

$$ds^2 = -dt^2 + a(t)^2 \delta_{ij} dx^i dx^j \quad (1.28)$$

where $a(t)$ is the scale factor. Using Einstein's equation, we can finally derive the background Friedmann equation as

$$\left(\frac{\dot{a}}{a}\right)^2 = \frac{8\pi G}{3} \bar{\rho}(t) \quad (1.29)$$

where the dot denotes a time derivative and $\bar{\rho}$ is the background energy density.

On this background, we want to consider a locally perturbed region that would eventually collapse into a black hole. For our purposes and considering the rarity of this kind of event, it may be approximated by a spherically symmetric region of positive curvature. Since the comoving size of this kind of region is initially much larger than the Hubble horizon size, we can assume the metric form as:

$$ds^2 = -dt^2 + a(t)^2 e^{2\psi(r)} \delta_{ij} dx^i dx^j \quad (1.30)$$

where $\psi > 0$ and is assumed to be monotonically decreasing to zero as $r \rightarrow \infty$. The above metric can be cast into the form of a locally closed Universe with the metric:

$$ds^2 = -dt^2 + a(t)^2 \left[\frac{dR^2}{1-K(R)R^2} + R^2 (d\theta^2 + \sin^2 \theta d\varphi^2) \right] \quad (1.31)$$

where the coordinates R and K are given by:

$$R = r e^{\psi(r)}; \quad K = -\frac{\psi'(r)}{r} \frac{2+r\psi'(r)}{e^{2\psi(r)}} \quad (1.32)$$

The 3-curvature of the $t = \text{constant}$ hypersurface is given by

$$R^{(3)} = -\frac{e^{-2\psi}}{3a^2} \delta^{ij} [2\partial_i \partial_j \psi + \partial_i \psi \partial_j \psi] = \frac{K}{a^2} \left(1 + \frac{d \ln K(R)}{3 d \ln R} \right) \quad (1.33)$$

Ignoring the spatial derivative of K , the time-time component of the Einstein equations (or the Hamiltonian constraint) gives

$$H^2 + \frac{K(r)}{a^2} = \frac{8\pi G}{3} \rho \quad (1.34)$$

where $H = \dot{a}/a$. This is basically equivalent to the Friedmann equation except for a small inhomogeneity induced by the curvature term. This inhomogeneity could be regarded as the Hamiltonian constraint on the comoving hypersurface or that on the uniform Hubble hypersurface on which the expansion rate is spatially homogeneous and isotropic. The above equation leads us to define the density contrast on the comoving hypersurface by

$$\Delta := \frac{\rho - \bar{\rho}}{\bar{\rho}} = \frac{3K}{8\pi G \bar{\rho} a^2} = \frac{K}{H^2 a^2} \quad (1.35)$$

On the other hand, we know that the radiation-dominated Universe is described by

$$\bar{\rho} \propto \alpha^{-3(1+w)}; \quad w = P/\bar{\rho} \quad (1.36)$$

where α is the scale factor and P is the pressure. The radiation era is described by $w = 1/3$ or α^{-4} . $\bar{\rho}(t)$ is infinitesimally small initially but this is consistent with the idea that it is the curvature perturbation that induces the density perturbation.

As the Universe continues to evolve, Δ grows to become of order unity. Ignoring the spatial dependencies, the Universe collapses when $K > 0$. This happens when the comoving scale of this positively curved region becomes of the order of the Hubble horizon scale and our previous approximations breaks down. However, we can use 1.34 to obtain an acceptable criterion for the black hole formation. This is also valid in fully nonlinear numerical studies.

If the Universe is isotropic and homogeneous, it stops expanding when $\Delta = 1$. So let us assume this epoch to be the time of black hole formation, $t = t_c$. At this point, we have to remember that perturbations on scales smaller than Jeans length cannot collapse so we set this to happen at $c_s^2 k^2 / a^2 = H^2$. Therefore, at the time of collapse, we have

$$1 = \Delta(t_c) = \frac{K}{k^2} \frac{k^2}{H^2 a^2} = \frac{K}{c_s^2 k^2} \quad (1.37)$$

The condition for black hole formation is that the comoving slice density contrast at the time when the scale of interest re-enters the Hubble horizon is greater than $\Delta_c = c_s^2$. This leads us to derive the following condition,

$$\Delta(t_k) = \frac{K}{H^2(t_k) a^2(t_k)} = \frac{c_s^2 k^2}{H^2(t_k) a^2(t_k)} \geq \Delta_c = c_s^2 = \frac{1}{3} \quad (1.38)$$

where t_k is the time at which $k/a = H$. Roughly, we can say that the mass of the formed PBH is equal to the horizon mass at the time of formation.

Power Spectrum of Primordial Density Perturbations

Most inflationary theories require a power spectrum of primordial density perturbations to be suitably large on certain scales that are associated with a particularly tuned background dynamics of the quantum fields in the early Universe. Primordial density perturbations from quantum fluctuations arose during the inflationary period of the Universe. This led to a nearly scale-invariant power spectrum [9] which was later confirmed by many cosmological measurements. Density and tensor perturbations evolve linearly and independently through the early Universe. However, they couple with each other non-linearly which leads to either non-Gaussianities or the stochastic background of GWs. ([10], [11]) If these density perturbations formed PBHs, it is possible to constrain primordial non-Gaussianities with PBHs. Alternatively, it's also interesting to search for PBHs through the measurement of the stochastic GW background. There have been studies about GWs induced from PBHs in the radiation-dominated era of the Universe that I will discuss in detail in section 1.6.

The power spectrum of primordial density perturbations can have a narrow major peak on small scales while it remains nearly scale-invariant on large scales as predicted by inflationary cosmology. Yet several minor peaks of the power spectrum on smaller scales can yield secondary contributions. Recently, [12] reported on a novel phenomenon of the resonance effect of primordial density perturbations called Sound Speed Resonance (SSR). This phenomenon describes the formation of PBHs caused by the resulting multiple peaks in the power spectrum. In [13], it was found that the formation of PBHs from the resulting peaks in SSR can be very efficient. The GWs induced within SSR at the sub-Hubble scales during inflation could become crucial at the critical frequency band due to a narrow resonance effect and hence, the spectrum of GWs with double peaks is typically predicted. [14] Thus, this phenomenon could potentially also be tested in future observational studies.

1.5.2 Non-Inflationary Scenarios

Besides the idea of density inhomogeneities forming as a result of inflation and leading to the formation of a PBH, there are many other theories that have been proposed over the years. These theories do not depend on the theory of inflation but rather describe other ways in which inhomogeneities could have formed. These include first-order phase transitions [15], bubble collisions [16], collapse of cosmic strings [17], necklaces [18], domain walls [19] and non-standard vacua [20]. The latter is of particular importance as it provides a natural scenario to get multi-modal PBH mass functions. [21]

1.5.3 Formation of PBH Binaries in the Present Universe

Previously, we discussed the formation of PBH binaries in the radiation-dominated era of the Universe. In addition to those PBHs, new PBH binaries can also form binaries in the present Universe.

Let us consider the possibility of a PBH traveling through the Universe and it comes into close interaction with another PBH. These PBHs may be freely moving through space or could be concentrated in large dark matter halos. This close interaction is illustrated in Fig. 1.4 where b is the impact parameter and r_p is the periastron. Dominant emission of gravitational waves

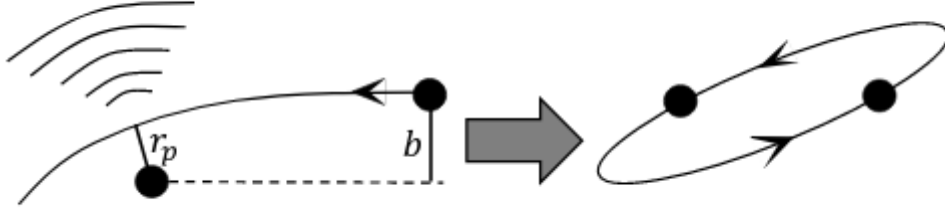


Figure 1.4: **Schematic representation of the close encounter of PBHs in the present Universe;** [8]

occur near the periastron where the relative acceleration of PBHs becomes the largest. If the amount of energy emitted in the form of GWs is greater than the kinetic energy of PBHs, the PBHs can escape and form a bound system instead. Alternatively, there could be a direct head-on collision between these two freely-moving PBHs but that is a probabilistically very unlikely.

In [22] and [8], they investigate this problem more quantitatively. According to [23], the time-averaged energy loss rate of the binary in the Keplerian orbit due to gravitational radiation is given by

$$\left\langle \frac{dE}{dt} \right\rangle = -\frac{32}{5} \frac{G^4 m_1^2 m_2^2 (m_1 + m_2)}{a^5 (1 - e^2)^{7/2}} \left(1 + \frac{73}{24} e^2 + \frac{37}{96} e^4 \right) \quad (1.39)$$

The energy loss during one orbital period T , using Kepler's third law, then becomes

$$\Delta E = -T \left\langle \frac{dE}{dt} \right\rangle = \frac{64\pi \sqrt{G(m_1 + m_2)} G^3 m_1^2 m_2^2}{5r_p^{7/2} (1 + e)^{7/2}} \left(1 + \frac{73}{24} e^2 + \frac{37}{96} e^4 \right) \quad (1.40)$$

Approximating the trajectory of the close encounter by $e = 1$, the energy loss becomes

$$\Delta E = \frac{85\pi \sqrt{G(m_1 + m_2)} G^3 m_1^2 m_2^2}{12\sqrt{2} r_p^{7/2}} \quad (1.41)$$

If this energy loss becomes greater than the kinetic energy $\mu v^2/2$, then the PBHs form a binary. (μ is the reduced mass and v is the relative velocity at large separation.) This imposes a condition on r_p as

$$r_p < r_{p,\max} = \left[\frac{85\pi}{6\sqrt{2}} \frac{G^{7/2}(m_1+m_2)^{3/2}m_1m_2}{v^2} \right] \quad (1.42)$$

In the Newtonian approximation, the relation between r_p and b is

$$b^2(r_p) = r_p^2 + \frac{2GM r_p}{v^2} \quad (1.43)$$

They finally conclude that in the limit of the strong gravitational focusing where $r_p \ll b$, the cross-section for forming a PBH binary becomes

$$\sigma = \pi b^2(r_{p,\max}) \simeq \left(\frac{85\pi}{3} \right)^{2/7} \frac{\pi (2GM_{\text{PBH}})^2}{v^{18/7}} \quad (1.44)$$

An interesting point to note here is that these PBH binaries are expected to merge before the age of the universe, as opposed to the PBH binaries formed in the radiation era.

1.6 Primordial Black Holes and Gravitational Waves

The first GW event GW150914 detected the merger of two $\sim 30 M_\odot$ mass BHs [3] in 2015. This led to renewed interest in PBHs and exploring the possibility that the LIGO detectors had actually detected PBHs and more importantly, PBHs that could account for dark matter. In one such paper [24], the authors concluded that although there are many theoretical uncertainties, the merger rate for $30 M_\odot$ PBHs, obtained with canonical models of dark matter distribution, does fall within the LIGO window. In [25], the authors also conclude that the event rate of mergers of PBH binaries falls into the range of the LIGO/Virgo network. Essentially, this means that these detectors could detect many PBH binaries during the observing runs.

Explaining the LIGO event by just PBHs is not trivial. For starters, since there is no inarguable evidence that they are not astrophysical source detections, we need to consider the PBH formation mechanism. This would help draw a clear distinction between the two different populations. Secondly, the PBH scenario needs to be matched with the existing constraints on the PBH abundance. The former problem is something we attempt to address in the second part of this thesis, although we focus only on the lower mass gap region. However, the analysis can be extended to higher or all mass ranges after further studies.

Recently, [26] suggested a model-independent approach for distinguishing between astrophysical black holes and primordial black holes. The main parameter that this study focuses

on is mass and more specifically, low masses. Stellar evolution models predict that black holes form only when a star's mass is sufficient for the gravitational force to overcome the degeneracy pressure. According to theoretical limits, black holes of stellar origin must have a mass greater than the Chandrasekhar limit i.e. $> 1.4M_{\odot}$. [27] A black hole below $1M_{\odot}$ must be of non-stellar origin and any detection in this mass range would be a smoking-gun detection. In principle, LIGO is sensitive to masses this low but there has been no detection so far. In Part I of this thesis, I discuss efficient methods to detect subsolar mass objects using the LIGO/Virgo search pipelines.

In the rest of this section, I discuss various aspects such as merger rates, PBH abundance and observational constraints that are instrumental in leading up to a GW detection. All of these parameters consist of many uncertain astrophysical factors but at the same time, these scenarios are roughly consistent with GW observations. In the coming decade, the sensitivity of GW interferometers will be greatly improved which will prove to be very helpful in establishing more confident information about PBHs.

1.6.1 Merger Event Rate of PBHs

Merger Event Rate in the Early Universe

PBH binaries that formed in the radiation era continuously emitted GWs. This meant that they continuously lost energy and began gradually shrinking to finally produce a merger. A binary consisting of point masses m_1 and m_2 with orbital parameters (a, e) merges due to gravitational radiation after a time t that is given by [23]

$$t = \frac{15}{304} \frac{a^4}{G^3 m_1 m_2 (m_1 + m_2)} \left[\frac{(1-e^2)}{e^{19}} \left(1 + \frac{121}{304} e^2 \right)^{\frac{870}{2299}} \right]^4 \int_0^e de' \frac{e'^{29}}{(1-e'^2)^{-\frac{3}{2}}} \left(1 + \frac{121}{304} e'^2 \right)^{\frac{870}{299}} \quad (1.45)$$

There are a few assumptions that are being made here, while deriving the merger rate. For starters, we assume that the binary is almost circular before merging ($e' = 0$). Secondly, $e \approx 1$ because the tidal force from the PBHs is negligible compared to the gravitational force between the PBHs that form the binary. This approximation greatly simplifies the above equation:

$$t = \frac{3}{85} \frac{1}{G^3 m_1 m_2 (m_1 + m_2)} (1 - e^2)^{7/2} a^4 \quad (1.46)$$

This expression implies that a highly eccentric binary merges in less amount of time than a circular binary with the same semi-major axis. This means that the binary radiates GWs dominantly around the periastron. Essentially, this implies that these PBH binaries merge within the age of the Universe.

Following the rest of the calculation in [25], the merger event rate \mathcal{R} per unit volume per unit time (at time t) is given by

$$\mathcal{R} = n_{\text{PBH}} \frac{dP}{dt} = \frac{3n_{\text{PBH}}}{58} \left(\frac{t}{T} \right)^{\frac{3}{8}} \left[\frac{1}{(1 - e_{\text{upper}}^2)^{\frac{25}{16}}} - 1 \right] \frac{1}{t} \quad (1.47)$$

where

$$t_c = T \left(\frac{4\pi f_{\text{PBH}}}{3} \right)^{\frac{37}{3}} \quad (1.48)$$

and

$$e_{\text{upper}} = \begin{cases} \sqrt{1 - \left(\frac{t}{T} \right)^{\frac{6}{37}}}, & \text{for } t < t_c \\ \sqrt{1 - \left(\frac{4\pi f_{\text{PBH}}}{3} \right)^2 \left(\frac{t}{t_c} \right)^{\frac{2}{7}}}, & \text{for } t \geq t_c \end{cases} \quad (1.49)$$

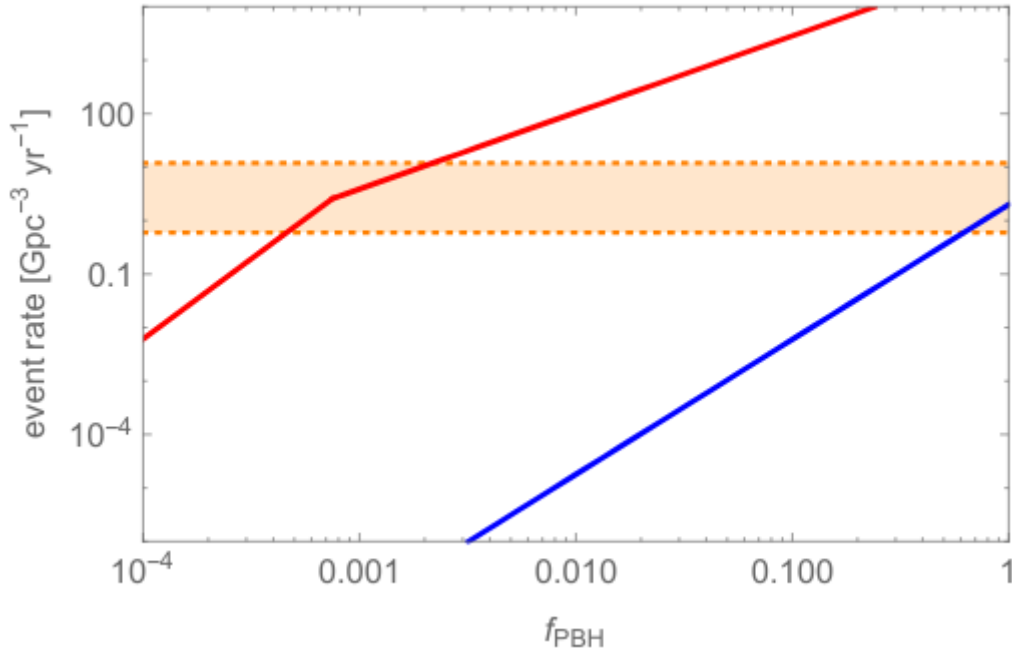


Figure 1.5: **Expected merger rates of PBH binaries**; The red (1.47) and blue (1.50) curves represent PBH binaries formed in the radiation era and present Universe respectively. [25]

Merger Event Rate in the Present Universe

The merger event rate of PBHs in the present Universe was estimated in [24]. The merger rate in this case is highly probabilistic and depends on the chance encounters of PBHs. Therefore, more PBH binaries are expected to form in highly dense regions. This suggests that a good place to look for PBHs would be inside low-mass dark halos that are dense regions with small virial velocity. The merger event rate was estimated based on three existing simulations to finally be

$$\mathcal{R} \approx 2\alpha f_{\text{PBH}}^{\frac{53}{21}} \text{Gpc}^{-3} \text{yr}^{-1} \quad (1.50)$$

This is the result for $M_{\text{PBH}} = 30M_{\odot}$. The value of α depends on the chosen simulation model and is 1 (*Press-Schechter*), 0.6 [28] and 10^{-2} [29] respectively. In 1.5, $\alpha = 1$ for the blue curve.

1.6.2 Abundance of PBHs

It is useful to introduce a new parameter β that represents the mass fraction of PBHs at formation while investigating the abundance of PBHs. This is defined as:

$$\beta := \left. \frac{\rho_{\text{PBH}}}{\rho_{\text{tot}}} \right|_{\text{at formation}} = \left(\frac{H_0}{H_{\text{form}}} \right)^2 \left(\frac{a_{\text{form}}}{a_0} \right)^{-3} \Omega_{\text{CDM}} f_{\text{PBH}} \quad (1.51)$$

where H is the Hubble parameters, f_{PBH} and Ω_{CDM} is the fraction of PBHs against total DM and the density parameter of the matter component at present respectively.

The mass of PBHs formed in the early universe (at formation) can be estimated by

$$\begin{aligned} M_{\text{PBH}} &= \gamma M_{\text{H}}|_{\text{at formation}} = \gamma \frac{4\pi}{3} \rho_{\text{form}} H_{\text{form}}^{-3} = \gamma \frac{4\pi}{3} \frac{3H_{\text{form}}^2}{8\pi G} H_{\text{form}}^{-3} \\ &= \gamma \frac{1}{2G} H_{\text{form}}^{-1} \end{aligned} \quad (1.52)$$

where a correction factor γ has been introduced. For simple analytic calculations, it can be assumed to be $\gamma \simeq 0.2$. [7]. Using the above equations, the mass fraction can be derived as

$$\beta \simeq 3.7 \times 10^{-9} \left(\frac{\gamma}{0.2} \right)^{-1/2} \left(\frac{g_{*, \text{form}}}{10.75} \right)^{1/4} \left(\frac{M_{\text{PBH}}}{M_{\odot}} \right)^{1/2} f_{\text{PBH}} \quad (1.53)$$

where g_* is the relativistic degrees of freedom. Thus, for each mass of PBHs, the observational constraint on f_{PBH} can be determined with β .

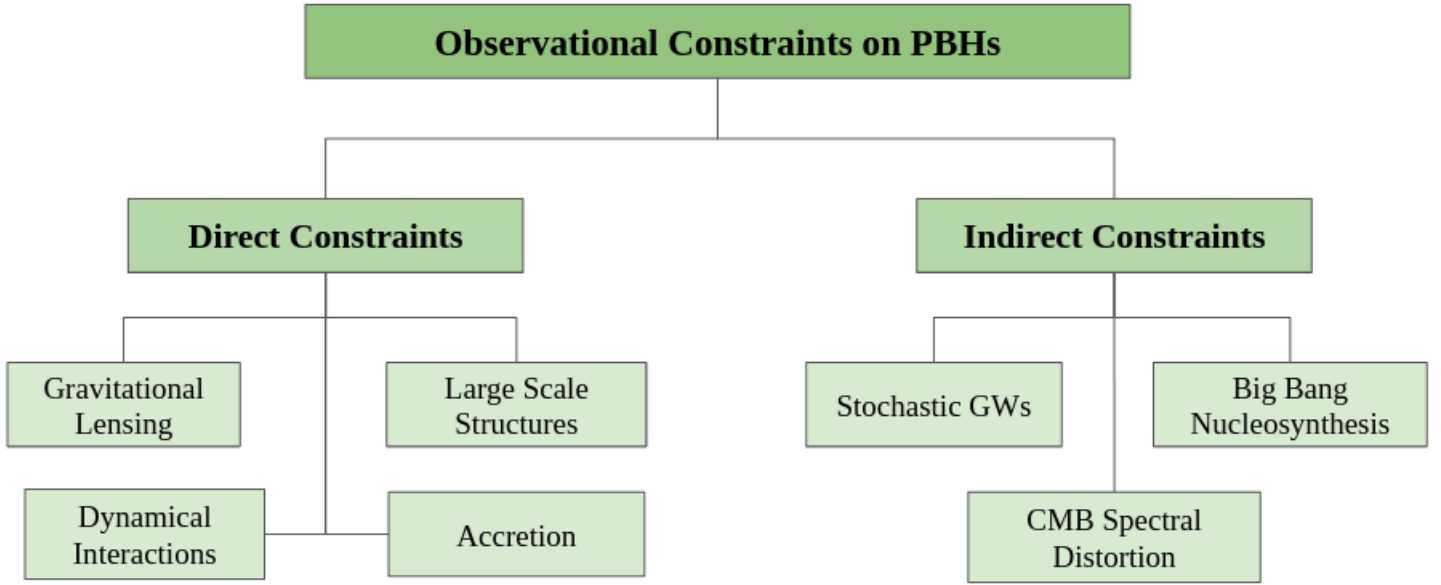


Figure 1.6: **Summary: Observational Constraints of PBHs;**

1.6.3 Observational Constraints on Non-Evaporating PBHs

While discussing the possibility of detecting a PBH, it is important to talk about the observational constraints. Broadly, the constraints are divided into **direct** and **indirect** ones. The direct observational constraints are derived by studying the effects that PBHs directly contribute to due to their gravitational potential. Consequently, these observations are independent of the PBH formation mechanism. On the other hand, indirect constraints are obtained by studying the observational effects that are not directly caused by PBHs but rather by something that is connected to a PBH. These indirect constraints are useful in confidently eliminating many possible PBH scenarios. Another important factor to consider is that the PBHs that we henceforth discuss have masses greater than $M_c = 10^{15}\text{g}$. PBHs lighter than this mass have already evaporated by the cosmic age t_0 due to Hawking radiation. [30]

$$M_c \simeq \left(\frac{3\hbar c^4 \alpha_0}{G^2} t_0 \right)^{\frac{1}{3}} \sim 10^{15}\text{g} \left(\frac{\alpha_0}{4 \times 10^{-4}} \right)^{\frac{1}{3}} \left(\frac{t_0}{13.8\text{Gyr}} \right)^{\frac{1}{3}} \quad (1.54)$$

For the rest of this subsection, I assume that the PBH mass function is monochromatic which is valid when the width of the mass function is sufficiently narrow. A summary of all the observational constraints can be found in Fig. 1.6.

Direct Observational Constraints on PBHs

1. **Gravitational Lensing:** One of the best and most relevant methods to detect PBHs is gravitational lensing. If PBHs are present in the Universe, they cause gravitational lensing on background objects like stars. GWs from binary black holes that are gravitationally lensed can be distorted by small microlenses along the line of sight. These microlenses that have masses of a few tens of solar masses can introduce a time delay of a few milliseconds. This sort of time delay would result in distinct interference patterns that can be measured with LIGO/Virgo.
2. **Dynamical Constraints:** Dynamical constraints simply arise from the fact that PBHs interact with their surroundings and disrupt existing astrophysical systems with their gravitational interactions. By evaluating the impact that PBHs have on these astrophysical systems, we can put an upper limit on PBH masses to a great extent. Many different astrophysical systems including the disruption of white dwarfs, neutron stars, wide halo binaries, globular clusters and ultra-faint dwarf galaxies have been studied so far. Another scenario that has been considered is the possibility of the Galactic center being composed of PBHs which undergo strong dynamical interactions with nearby stars. Eventually, these objects would lose enough kinetic energy to spiral into the center of the galaxy. Finally, this would result in a highly concentrated Galactic center, comprising of PBHs. This would also comply with certain dark matter theories related to Galactic halos.
3. **Accretion Constraints:** The accretion of gas onto the PBHs has a significant effect on the PBH abundance constraint. Broadly, there are two main processes that contribute to this constraint - accretion effects due to the CMB in the early Universe and the electromagnetic waves from the accreted matter of PBHs.
4. **Large Scale Structure Constraint:** There are multiple cosmological theories that attempt to explain the formation of large structures in the Universe from first principles. However, it remains largely unexplained. Previously, this was explained by primeval fluctuations from the hot Big Bang. In [31], the idea that black holes from the early Universe contribute to the formation of large structures like galaxies was first proposed.

Indirect Observational Constraints on PBHs

1. **Stochastic GWs from Primordial Density Perturbations:** If we assume that primordial density perturbations existed on super-Hubble scales, the production of the stochastic GW backgrounds happens when these perturbations re-enter the Hubble horizon. [10] In other words, this means that the GWs are produced at the same epoch as the PBH formation. The GWs have ultra-low frequencies in the nHz band and can potentially be constrained by pulsar timing experiments.
2. **CMB Spectral Distortions:** The primordial density perturbations generate spectral distortions in the CMB. This happens when the perturbations of photons and baryonic gases re-enter the Hubble horizon prior to the CMB decoupling. These perturbations undergo acoustic oscillations due to the tight coupling between photons and baryons. [32] This forms a source for indirect constraints.

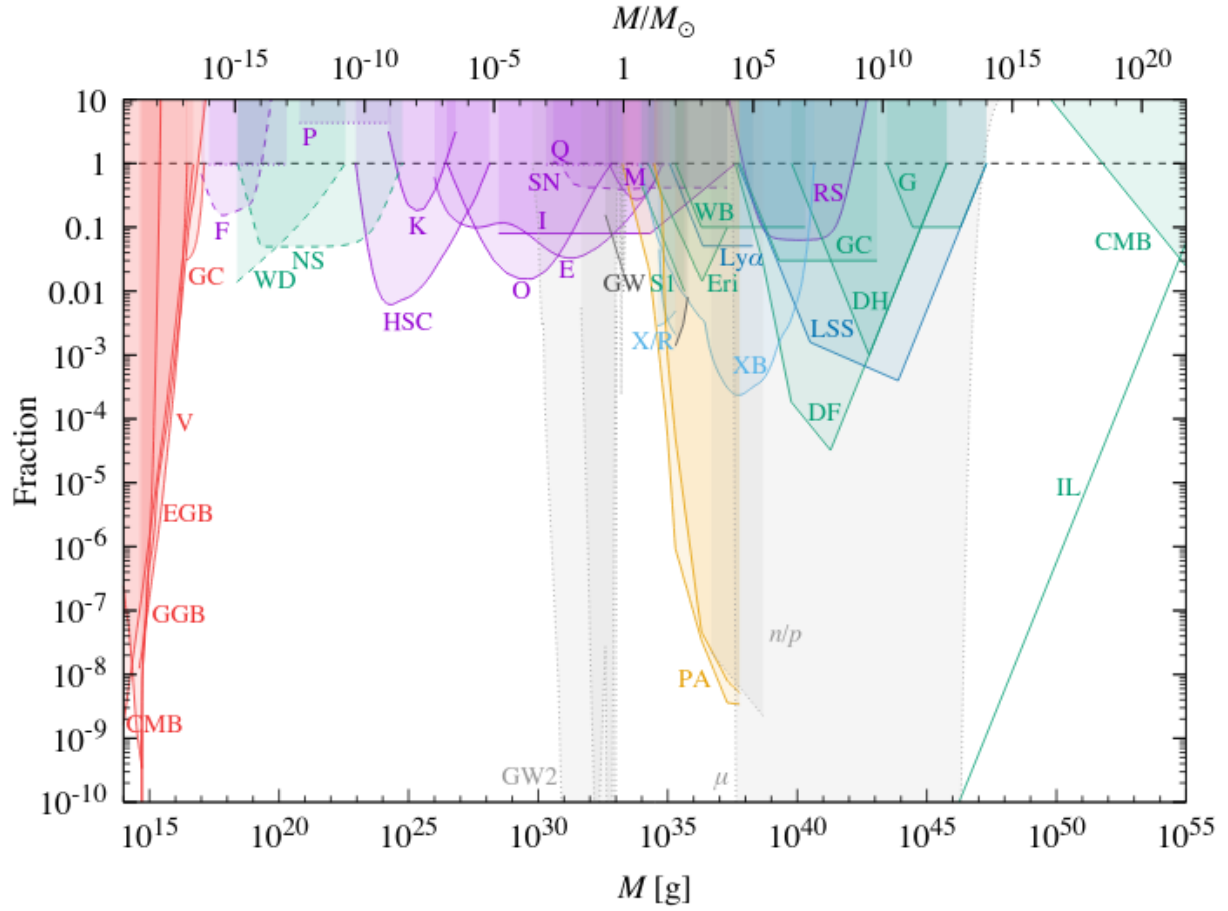


Figure 1.7: **Summary of all PBH Constraints (Carr 2020)** [33]; Constraints from evaporation (red), lensing (magenta), dynamical effects (green), accretion (light blue), CMB distortions (orange), large-scale structures (dark blue) and background effects (grey). Broken lines indicate constraints that are possibly incorrect while dotted lines indicate constraints depend on additional assumptions.

1.7 Primordial Black Holes as Dark Matter

The notion that PBHs could potentially explain all or a part of dark matter has been extensively studied over the years. PBHs are ideal candidates for dark matter, considering their non-luminous, non-relativistic and nearly collision-less nature. The unexpected large mass of GW150914 [3] and GW170814 [34] combined with the inferred merger rate coinciding with PBH abundances comparable to DM [24] [35] revived interest in PBHs as potential DM candidates.

In [36], the authors describe seven main hints for considering PBHs as DM. The seven hints are namely: the rate and mass of BBH mergers detected by LIGO/Virgo; spin measurements of the detected events; detection of microlensing of distant quasars and stars in M31; distribution and dynamics of faint dwarf galaxies and of their stellar clusters; evidence for cored DM profiles on different halo mass scales; observation of a population of SMBH in the early universe; spatial correlations of the source-subtracted CIB; and soft X-ray background fluctuations. While all these phenomena can be explained by other astrophysical theories as well, it is interesting to note that the explanation of PBHs as DM can single-handedly explain them all.

In [24], the authors show that if DM consisted of $\approx 30M_{\odot}$ BHs, analogous to the first LIGO detection [3], then the rate for mergers of PBHs falls within the inferred merger rate. This would essentially imply that LIGO has already detected DM. While they do not confidently conclude this claim, they do mention that this possibility cannot be ruled out. Numerous studies have concluded that subsolar mass PBHs cannot account for all of DM but rather, only for a fraction of it. This conclusion stems from the fact that these PBHs would greatly surpass the observed LIGO/Virgo rates. However, in a very recent paper [37], the author shows this assumption to be incorrect and stresses upon the idea that PBHs formed from QCD transitions may constitute all of DM. Another recent study [38] focused on LIGO/Virgo measurements concluded that in the absence of accretion, PBHs can be ruled out entirely. In simple words and as a concluding remark, it is suffice to say research in this area is still very open-ended with many unanswered questions and numerous novel things to consider.

PART I: IMPROVING SUB-SOLAR MASS SEARCHES FOR PRIMORDIAL BLACK HOLES

2.1 Introduction

Progress in the development of data analysis methods for detection of GWs, and the advancement of detectors are of fundamental importance for the evolution of GW astronomy. Developments in both GW data analysis and an increment in GW detectors are both driven by the idea of maximizing the detection rate of GW events. Additionally, an extended network of GW observatories facilitates the dawn of multi-messenger astronomy leading to the availability of more data that needs to be analyzed. Together, with the addition of new detectors and extended observatories, an unprecedented amount of data will be produced. Furthermore, *low-latency*¹ searches are essential for speedy astrophysical counterpart follow-ups of the GW detections. Another factor to consider is that the increase in the degrees of freedom of the CBC search space to include more parameters such as spin precession, effects of non-circular orbit in templates will increase the overall number of templates required by many orders. This along with the fact that more detectors will reach design sensitivity, will lead to highly dense templates. Essentially, this means that we can expect more number of highly dense templates to analyze, leading to high computational costs and long run-times. Overall, GW data analysis techniques face a constant challenge and urgently require accelerated upgradation.

The lightest ultracompact objects are formed when stellar remnants exceed the Chandrasekhar mass limit i.e. $\sim 1.4M_{\odot}$. Some equations of state predict the stability of neutron stars at masses as low as $\sim 0.1M_{\odot}$. However, there is no theory predicting the formation of neutron stars below $\sim 1M_{\odot}$. On the other hand, the observational minimum mass limit of black holes is $\sim 5M_{\odot}$. Ultimately, we can conclude that no conventional stellar evolution models predict the existence of astrophysical objects in the sub-solar mass region ($<1M_{\odot}$). Alternatively, we do know that primordial black holes can exist over all mass ranges [7], including the sub-solar region. Hence, any event in this range would be a smoking gun detection. This is the aspect we focus on in this chapter.

The number of templates we would need for a sub-solar mass template bank is given by

$$N \propto m_{\min}^{-8/3} f_{\min}^{-8/3}, \quad (2.1)$$

where m_{\min} is the minimum mass included in the search and f_{\min} denotes the starting frequency of the template waveforms. [39] If we consider $m_{\min} = 0.1M_{\odot}$, we would need *at least* 10^3 more templates since $N \sim 10^3$. Therefore, the main problems that we would face while trying to analyze such low-mass waveforms are the high computational costs and the long duration that it would take to run. In our case, we would directly benefit from better analysis techniques and it is worth taking a better look at the methods employed by CBC search pipelines within the LVC.

¹The time taken between the arrival of the GW at the detectors and the GW event detection.

The `gstLAL` search pipeline makes use of the Singular Value Decomposition (SVD) method. It reduces the number of filters required when analyzing GW data for CBC signals. [40] In this chapter, I discuss another method called Random-Projection Singular Value Decomposition (RSVD) [41] which could potentially be a better method compared to SVD. RSVD includes a powerful data reduction method called Random Projections (RP), in the matched filtering search of CBCs. We discuss the two methods in detail (2.1.2, 2.2) and also draw a comparison between the two (2.3). The final goal of this kind of project would be to incorporate the better method into the relevant search pipelines.

2.1.1 GstLAL Search Pipeline

The `GstLAL` search pipeline is a low-latency, multi-detector matched-filtering technique to search for GWs from CBCs. It utilizes time-domain operations, leading to a low-latency of seconds which is helpful when analyzing binary neutron star (BNS) events. BNS events always have an electromagnetic counterpart whereas PBH mergers are not expected to have any. In our case, this proves to be relevant when differentiating sub-solar mass PBHs from low-mass BNS systems.

Figure 2.1 displays the rudimentary structure of the search pipeline and its three main steps. Our main focus is making a change in the first step: **replacing SVD with RSVD**. The following steps remain approximately the same, with small changes that we discuss later in the chapter.

2.1.2 Singular Value Decomposition (SVD)

One of the main data analysis challenges that are faced while searching for CBCs using the matched-filtering technique is the *data redundancy* problem. The template placement algorithms use a criterion called *minimal match* to distribute the template waveforms in a bank. This ensures that the neighbouring templates have significant overlap (>95%) to avoid the loss of any event data because of the discreteness of the parameters in the templates. The minimal match criterion means that high-redundancy exists in the template bank which means that a high number of correlated calculations are required while filtering the data with the template bank. A convenient approach to this problem is by employing linear algebra methods that perform data reduction such as Singular Value Decomposition (SVD). In this subsection, we are going to look at the detailed steps of SVD and understand how the method works in detail.

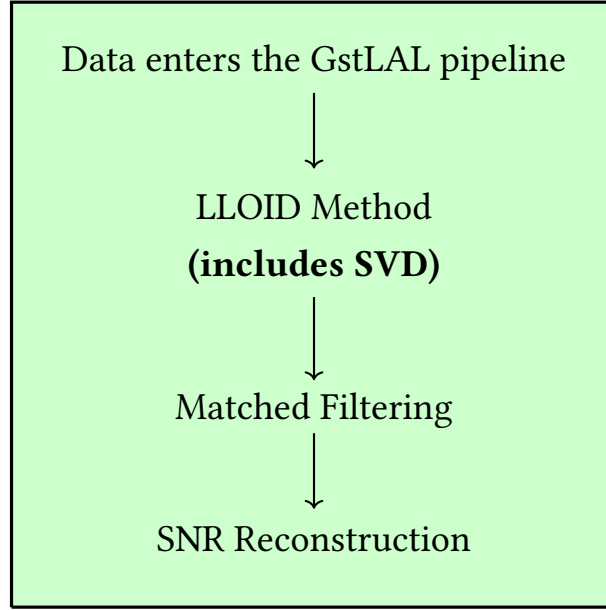


Figure 2.1: **Rudimentary Structure of the GstLAL Pipeline**

Let us define a vector a and also consider its transpose a^T :

$$a = \begin{pmatrix} \alpha_x \\ \alpha_y \end{pmatrix}; \quad a^T = (\alpha_x \quad \alpha_y). \quad (2.2)$$

We define the projection direction vectors as:

$$v_1 = \begin{pmatrix} v_{1x} \\ v_{1y} \end{pmatrix}; \quad v_2 = \begin{pmatrix} v_{2x} \\ v_{2y} \end{pmatrix}. \quad (2.3)$$

Next, we define the projection lengths $S_{\alpha 1}$ and $S_{\alpha 2}$ as

$$S_{\alpha 1} = a^T \cdot v_1 = (\alpha_x \quad \alpha_y) \cdot \begin{pmatrix} v_{1x} \\ v_{1y} \end{pmatrix}, \quad (2.4)$$

and

$$S_{\alpha 2} = a^T \cdot v_2 = (\alpha_x \quad \alpha_y) \cdot \begin{pmatrix} v_{2x} \\ v_{2y} \end{pmatrix}. \quad (2.5)$$

If we generalize the matrices V and S as

$$V = \begin{pmatrix} v_{1x} & v_{2x} \\ v_{1y} & v_{2y} \end{pmatrix}; \quad S = (S_{\alpha 1} \quad S_{\alpha 2}), \quad (2.6)$$

we have the general expression as

$$a^T \cdot V = S. \quad (2.7)$$

In essence, we have

$$\begin{aligned} S &= A.V \\ \implies A &= SV^{-1} \\ A &= S.V^T. \end{aligned} \quad (2.8)$$

The SVD formula is finally given by

$$\boxed{A = U\Sigma V^T} \text{ where } S = U\Sigma. \quad (2.9)$$

To understand this better, let us consider the 2-dimensional S matrix again:

$$\begin{pmatrix} S_{\alpha 1} & S_{\alpha 2} \\ S_{\beta 1} & S_{\beta 2} \end{pmatrix}, \quad (2.10)$$

where the magnitude of each column is given by

$$\begin{aligned} \sigma_1 &= \sqrt{(S_{\alpha 1})^2 + (S_{\beta 1})^2} \\ \sigma_2 &= \sqrt{(S_{\alpha 2})^2 + (S_{\beta 2})^2}. \end{aligned} \quad (2.11)$$

Using this, we can rewrite S as

$$S = \begin{pmatrix} \frac{S_{\alpha 1}}{\sigma_1} & \frac{S_{\alpha 2}}{\sigma_2} \\ \frac{S_{\beta 1}}{\sigma_1} & \frac{S_{\beta 2}}{\sigma_2} \end{pmatrix} \cdot \begin{pmatrix} \sigma_1 & 0 \\ 0 & \sigma_2 \end{pmatrix} = \begin{pmatrix} U_{\alpha 1} & U_{\alpha 2} \\ U_{\beta 1} & U_{\beta 2} \end{pmatrix} \cdot \begin{pmatrix} \sigma_1 & 0 \\ 0 & \sigma_2 \end{pmatrix}, \quad (2.12)$$

where

$$U = \begin{pmatrix} U_{\alpha 1} & U_{\alpha 2} \\ U_{\beta 1} & U_{\beta 2} \end{pmatrix} \text{ and } \Sigma = \begin{pmatrix} \sigma_1 & 0 \\ 0 & \sigma_2 \end{pmatrix}. \quad (2.13)$$

Now that we have a general expression, let us extend this to more vectors and consider a multi-dimensional vector A for the remaining derivation:

$$A = \begin{pmatrix} \alpha_x & \alpha_y & \cdots \\ \beta_x & \beta_y & \cdots \\ \vdots & \vdots & \ddots \end{pmatrix} \quad (2.14)$$

Following Eqn. 2.7, we have

$$\begin{pmatrix} \alpha_x & \alpha_y & \cdots \\ \beta_x & \beta_y & \cdots \\ \vdots & \vdots & \ddots \end{pmatrix}_{n \times d} \cdot \begin{pmatrix} v_{1x} & v_{2x} & \cdots \\ v_{1y} & v_{2y} & \cdots \\ \vdots & \vdots & \ddots \end{pmatrix}_{d \times d} = \begin{pmatrix} S_{\alpha 1} & S_{\alpha 2} & \cdots \\ S_{\beta 1} & S_{\beta 2} & \cdots \\ \vdots & \vdots & \ddots \end{pmatrix}_{n \times d}, \quad (2.15)$$

where n is the number of points and d is the number of dimensions.

We consider the multi-dimensional S matrix:

$$\begin{pmatrix} S_{\alpha 1} & S_{\alpha 2} & \cdots \\ S_{\beta 1} & S_{\beta 2} & \cdots \\ \vdots & \vdots & \ddots \end{pmatrix}, \quad (2.16)$$

Following Eqn. 2.11, we can write the general expression for the magnitude of each column as

$$\sigma_n = \sqrt{(S_{\alpha n})^2 + (S_{\beta n})^2 + \cdots + (S_{dn})^2}. \quad (2.17)$$

We can now rewrite Eqns. 2.12 and 2.13 as:

$$\begin{pmatrix} \frac{S_{\alpha 1}}{\sigma_1} & \frac{S_{\alpha 2}}{\sigma_2} & \cdots & \frac{S_{\alpha n}}{\sigma_n} \\ \frac{S_{\beta 1}}{\sigma_1} & \frac{S_{\beta 2}}{\sigma_2} & \cdots & \frac{S_{\beta n}}{\sigma_n} \\ \vdots & \vdots & \ddots & \vdots \\ \frac{S_{d1}}{\sigma_1} & \frac{S_{d2}}{\sigma_2} & \cdots & \frac{S_{dn}}{\sigma_n} \end{pmatrix} \cdot \begin{pmatrix} \sigma_1 & 0 & 0 & 0 \\ 0 & \sigma_2 & 0 & 0 \\ \vdots & \vdots & \ddots & \vdots \\ 0 & 0 & 0 & \sigma_n \end{pmatrix} = \begin{pmatrix} U_{\alpha 1} & U_{\alpha 2} & \cdots & U_{\alpha n} \\ U_{\beta 1} & U_{\beta 2} & \cdots & U_{\beta n} \\ \vdots & \vdots & \ddots & \vdots \\ U_{d1} & U_{d2} & \cdots & U_{dn} \end{pmatrix} \cdot \begin{pmatrix} \sigma_1 & 0 & 0 & 0 \\ 0 & \sigma_2 & 0 & 0 \\ \vdots & \vdots & \ddots & \vdots \\ 0 & 0 & 0 & \sigma_n \end{pmatrix}, \quad (2.18)$$

where

$$U = \begin{pmatrix} U_{\alpha 1} & U_{\alpha 2} & \cdots & U_{\alpha n} \\ U_{\beta 1} & U_{\beta 2} & \cdots & U_{\beta n} \\ \vdots & \vdots & \ddots & \vdots \\ U_{d1} & U_{d2} & \cdots & U_{dn} \end{pmatrix} \text{ and } \Sigma = \begin{pmatrix} \sigma_1 & 0 & 0 & 0 \\ 0 & \sigma_2 & 0 & 0 \\ \vdots & \vdots & \ddots & \vdots \\ 0 & 0 & 0 & \sigma_n \end{pmatrix}. \quad (2.19)$$

2.2 Random Projection-Based Singular Value Decomposition (RSVD)

2.2.1 Random Projections (RP)

Previously, we discussed the data growth in GW astronomy due to the addition of new detectors and multi-messenger astronomy and also the concern this puts on most existing data analysis techniques. While data reduction methods like SVD are used in certain search pipelines like GstLAL, it does not scale favourably with the increase in data. We need more efficient methods to alleviate the effects of redundancy and higher dimensionality of the GW database. There are multiple methods for dimensionality reduction, including SVD but Random Projections (RP) is the only method that's data-independent and consequently, is capable of solving the redundancy problem while keeping the computational costs low.

RP involves choosing a random subspace for the projection of data from a significantly high-dimensional² space. (Fig. 2.2) The mapping from high-dimensional space to lower-dimensional space is achieved by simply multiplying the data with a random matrix. It is important to note that the dimension of the data corresponds to the number of variable in the data. The lower-dimensional space is then utilized for the analysis. It not only keeps the costs low but it also preserves the original structure³ of the data leading to a a minimal loss of event data.

Theoretical Origin of RP

RP is based on the Johnson-Lindenstrauss lemma [42] which guarantees that in Euclidean space, there always exists a projection from high-dimensional data to low-dimensional data that satisfies distortion conditions with high probability.

Johnson-Lindenstrauss Lemma

Lemma 2.2.1 *For any dataset of n points, $\mathcal{V} = \{x_1, x_2, \dots, x_n\}$ in \mathbb{R}^d , any $0 < \epsilon < 1$, let k be a positive integer such that*

$$k \geq \frac{4 \log n}{\epsilon^2/2 - \epsilon^3/3} \quad (2.20)$$

then, there exists a linear map $f : \mathbb{R}^d \rightarrow \mathbb{R}^k$ such that $\forall x_i, x_j \in \mathcal{V}$, with very high probability we have

$$(1 - \epsilon) \|x_i - x_j\|^2 \leq \|f(x_i) - f(x_j)\|^2 \leq (1 + \epsilon) \|x_i - x_j\|^2 \quad (2.21)$$

²Dimension of the data corresponds to the the number of variables in the data;

³Structure of the data depends on the context of the discussion - in templated matched filtering CBC searches, it is represented by the Euclidean distance between different points of a given database;

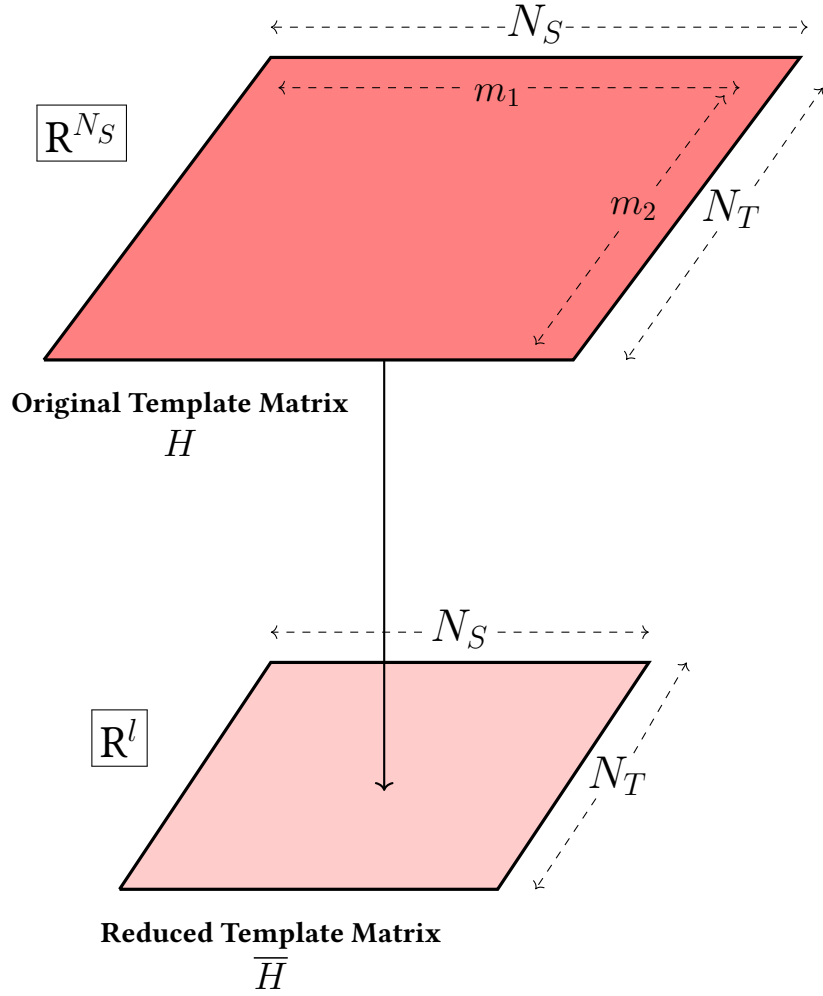


Figure 2.2: **Schematic diagram to show the projection of data from a high-dimensional space \mathcal{R}^{N_S} (original template bank) to a lower-dimensional space \mathcal{R}^l (reduced template bank);** For better understanding, the spaces can be understood as matrices where each row contains a template (N_T) and each column contains a sample point (N_S) of the waveform in the template. The parameter space \mathcal{R}^{N_S} contains physical attributes - in this case, masses m_1 and m_2 whereas the \mathcal{R}^l space is independent of physical attributes.

RP of GW-Templates

The reason RP is a great dimensionality reduction method is because it preserves embedding. This means that the Euclidean distance between two data points in Euclidean space is preserved even when it is mapped onto a lower-dimensional subspace. By Euclidean distance, we precisely mean the distance dS^2 between two data points. The GW template banks are Euclidean in nature and hence, RP can be effectively applied since the data structure will be preserved under RP of the template bank to a lower-dimensional space.

2.2.2 Generating a Random Matrix

The J-L lemma above describes a linear map f which describes a mapping between two Euclidean spaces of different dimensions. The main question here is - what is f and how can it be defined? This proves to be a very complicated mathematical procedure. However, in our case, f can also be understood as a random matrix Ω which is a function that maps a higher-dimensional space to a lower-dimensional space. This "embedding function" f or Ω is simply a Gaussian matrix.

The elements of Ω matrix are drawn independently and identically from a Gaussian distribution with mean zero and variance $1/k$, i.e. $\mathcal{N}(0, 1/k)$. The Gaussian random matrix Ω is quasi-orthonormal such that $\langle \Omega \Omega^T \rangle = I$. Thus, the transformation preserves the relationship between the pairs of data vectors with significant degree of accuracy. The choice of the embedding function f makes RP a simple, universal and very powerful method of reducing the dimension of data in Euclidean space.

2.2.3 Randomized-SVD

Let us consider a template matrix \mathbf{H} in a higher-dimensional space \mathbb{R}^{N_s} . An embedding function f is used to transform this matrix into a new smaller matrix $\bar{\mathbf{H}}$ in a lower-dimensional space \mathbb{R}^l . In the next step, *QR decomposition*⁴ is employed and the new template matrix $\bar{\mathbf{H}}$ is used for it. Finally, we get back the B matrix which we proceed to use for matched filtering. The RSVD technique is summarized in detail on the following page.

⁴QR decomposition is similar to SVD;

2.2.4 Summary Page of RSVD

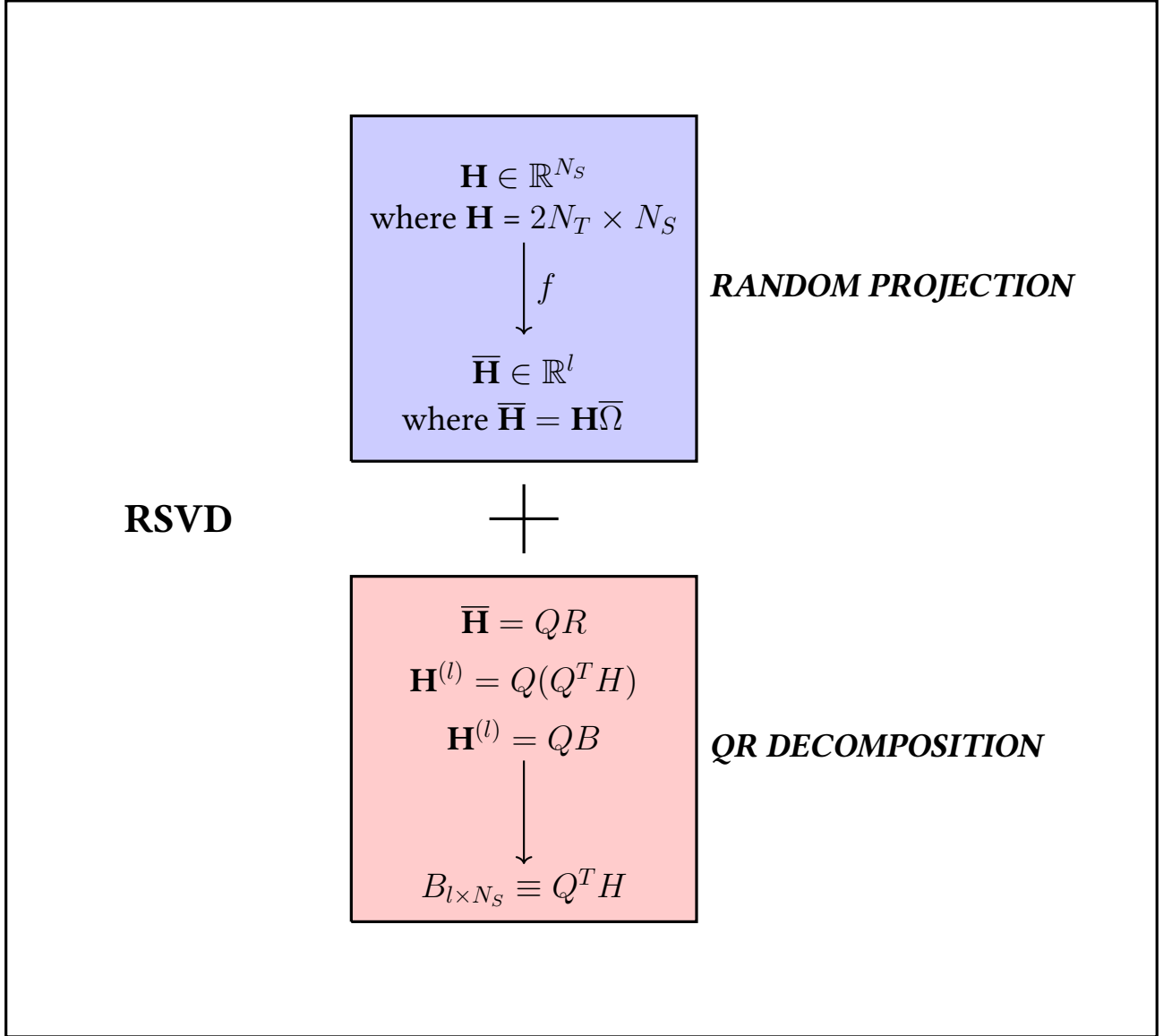


Figure 2.3: **Schematic Diagram of RSVD**

l	$\sim \mathcal{O}(\log(2N_T)/\epsilon^2)$
ϵ	$0 < \epsilon < 1$
\mathbf{H}	$= 2N_T \times N_S$

\mathbf{H}	template matrix
N_T	number of templates
N_S	sample points
\mathbb{R}^{N_S}	N_S -dimensional Euclidean space
\mathbb{R}^l	l -dimensional randomly generated subspace
ϵ	mismatch/distortion factor after projection
$\bar{\mathbf{H}}$	template matrix in lower-dimensional Euclidean space
$\bar{\Omega}$	random matrix
Q	orthonormal matrix with $2N_T \times l$ dimensions
B	orthonormal projection of template waveforms into the compressed subspace

2.2.5 What do we do with the \mathbf{B} matrix?

$$\mathbf{B}_{l \times N_S} \equiv \mathbf{Q}^T \mathbf{H} \quad (2.22)$$

The matrix \mathbf{B} defines the orthonormal projection of the template waveforms into the compressed subspace. We can use the l rows of \mathbf{B} as surrogate templates which can be used to correlate against the detector data \vec{S} . We can simply understand the l rows as filters. And hence, the next thing we do with the \mathbf{B} matrix is proceed to perform matched filtering.

2.2.6 SNR Reconstruction

Introduction

The template bank consists of templates of alternating polarizations. This implies that every alternate template corresponds to plus-polarization and the others to cross-polarization. Hence, the phase shift between any two consecutive templates in the template bank is always 90 degrees. The phase shift can then be maximized over all space to get a complex matched filter output.

Template banks can be made up of either intrinsic or extrinsic parameter spaces (templates):

Extrinsic Space: If there is an overlap between two templates when maximized over extrinsic parameters, it produces a **match**.

Intrinsic Space: If there is an overlap between two templates when maximized over intrinsic parameters, it produces **rank deficiency**. GW searches are usually done over intrinsic parameter space.

Typically, CBC searches involve calculating the cross-correlation between \vec{S} and every row of \mathbf{H} for a series of relative time-shifts, generating a time-series of ρ_α values, for every α .

But why do we need reconstruction?

The original \mathbf{H} exists in a large parameter space, described by intrinsic parameters like mass and spin. (In our case, only the component masses m_1 and m_2). Using SVD or RSVD, we reduce this large parameter space into a smaller subspace \mathbf{H} or $\mathbf{H}^{(l)}$ which has no physical attributes or parameters. So after we have finished our work within the smaller subspace, we need to reconstruct it back into the original space to correlate the data with the physical parameters. However, since there is always a loss of data while using SVD or RSVD, it is

nearly impossible to get back our original matrix exactly. However, the reconstructed matrix will be approximately equal to the original matrix.

Reconstruction of SNR in SVD

The rank deficiency of \mathbf{H} is exploited in the truncated SVD approach - which means that singular values can be truncated and the template bank can be made smaller overall. To be precise, $(2N_T - l)$ singular values are discarded from the original template matrix. And hence, the reconstructed fractional SNR loss can be measured as a function of these discarded values.

The SNR of the α -th row of the template bank is given by

$$\rho_\alpha = (H_{(2\alpha-1)} - iH_{(2\alpha)})\vec{S}^T \quad (2.23)$$

where $H_{(2\alpha-1)}$ and $H_{(2\alpha)}$ are rows (slices) of the template matrix \mathbf{H} ; \vec{S}^T is the transpose of the whitened signal data.

The average fractional SNR loss (or the truncation) is given by:

$$\left\langle \frac{\delta\rho}{\rho} \right\rangle \leq \frac{\|\mathbf{H}\|_F^2 - \|\mathbf{H}^{(l)}\|_F^2}{\|\mathbf{H}\|_F^2} \quad (2.24)$$

Reconstruction of SNR in RSVD

The rank- l matrix factorization of \mathbf{H} using RSVD is given by $\mathbf{H}^{(l)} = QB$. Hence, the SNR ρ_α' for any given time t_0 can be reconstructed in \mathbb{R}^{N_S} as

$$\rho_\alpha = (H_{(2\alpha-1)} - iH_{(2\alpha)})\vec{S}^T = \sum_{\nu=1}^l (Q_{(2\alpha-1)\nu} - iQ_{(2\alpha)\nu}) (B_\nu \vec{S}^T) \quad (2.25)$$

Using both Pythagoras theorem and the relation $\|\mathbf{H}\|_F^2 - 2N_T$, the average fractional loss of SNR is given by

$$\left\langle \frac{\delta\rho}{\rho} \right\rangle \leq \frac{\|\mathbf{H}\|_F^2 - \|\mathbf{H}^{(l)}\|_F^2}{\|\mathbf{H}\|_F^2} = 1 - \frac{\sum_{\mu=1}^l \sigma_\mu^2}{2N_T} \quad (2.26)$$

2.3 Comparison between SVD and RSVD

The SVD and RSVD methods were extensively discussed in the previous sections, they can be briefly summarized as:

SVD

1. Define a vector \vec{a} and transpose it to get \vec{a}^T .
2. Define projection direction unit vectors \vec{v}_1, \vec{v}_2 and projection lengths $\vec{S}_{a1}, \vec{S}_{a2}$.
3. Write in the form of $\vec{a}^T \cdot V = S$
4. Extend it to more vectors i.e. more number of points and dimensions to basically get $A = SV^T$;
(A: vector of $n \times d$ dimensions, V: projection direction unit vectors of dimension $d \times d$ and S: projection length vector of $n \times d$ dimensions)
5. The SVD formula is given by $A = U\Sigma V^T$ which implies that $S = U\Sigma$.
(Σ is a vector of the magnitude values of the S matrix columns)
6. Matrix V is used to correlate the data and S is used for reconstruction.

RSVD

1. We have $2N_T$ vectors in \mathbb{R}^{N_S} , describing the template matrix \mathbf{H} where $\mathbf{H} = 2N_T \times N_S$
2. The individual row-vectors of \mathbf{H} are mapped into a randomly generated subspace \mathbb{R}^l using $\vec{\Omega}_{N_S \times l} \in \mathcal{N}(0, 1/l)$
3. We get $\vec{\mathbf{H}}_{2N_T \times l} = \mathbf{H}\vec{\Omega}$ where Ω is the random matrix.
4. $\vec{\mathbf{H}}$ can now be used for SVD-like operations i.e. QR decomposition. [43]
5. We obtain a matrix B after decomposition, the rows of this matrix can be treated as filters and be used to correlate the data.

The current gstLAL pipeline divides the template banks into smaller "split-banks". Each split-bank contains templates of similar time-frequency evolution. And then, SVD is performed individually on each split-bank. However, RSVD reduces the entire template matrix space to a subspace and performs the decomposition operation only once. This could potentially cure the redundancy problem to a large extent.

The next step would be to draw a comparison between the two and gauge which might be better in terms of run-time, computational costs and percentage of data loss. To do this, we used a test bank comprised of 40526 templates of binary neutron star (BNS) mergers in the mass range $1.42 - 1.69 M_{\odot}$ as shown in Fig. 2.4. The reason for choosing BNS merger templates is that these waveforms are very similar to the subsolar mass region waveforms, in terms of length. Hence, this would enable us to make a good approximation and better understand what to expect from the two methods.

1. **Run-Time:** Using the test template bank, I ran both SVD and RSVD and checked the time taken for either method to finish running. There was a clear winner in this case with the RSVD method running $\sim 18\times$ faster than SVD. The exact numerical difference is shown below

Time Elapsed (s)	
SVD	954.33
RSVD	51.95

2. **Computational Costs:**

If $N_T \leq N_S$, the computational costs are given by:

$$\text{SVD: } \mathcal{O}(N_T^2 N_S), \quad [40] \quad (2.27)$$

$$\text{RSVD: } \mathcal{O}(\ell N_T N_s + (\ell^2 N_T - \frac{2}{3} \ell^3) + \ell N_T N_s + \ell N_s), [41] \quad (2.28)$$

In both cases, $N_T = 40526$ and $N_S = \ell = 2049$ which leads to the respective computational costs being calculated as

Computational Costs	
SVD	$\mathcal{O}(10^{13})$
RSVD	$\mathcal{O}(10^{12})$

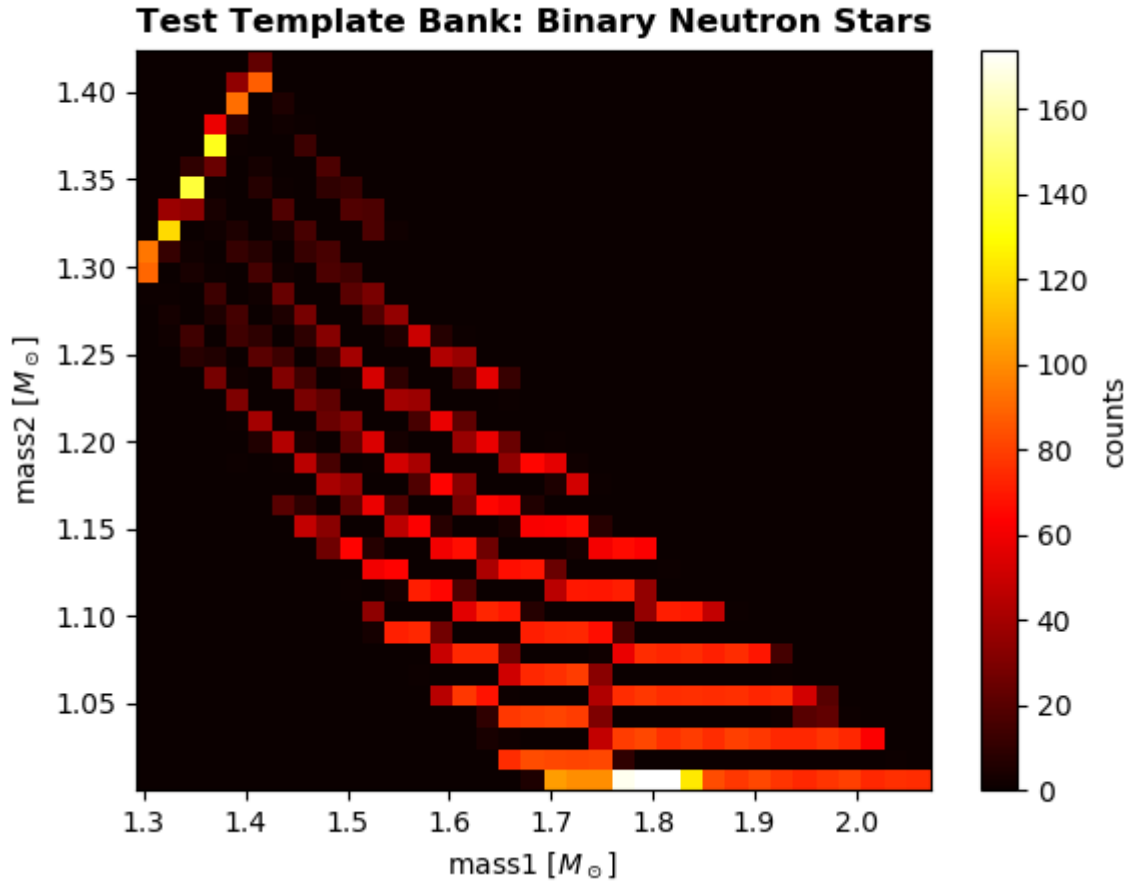


Figure 2.4: **Test Template Bank of Binary Neutron Stars**, containing 40526 templates;
Mass Range: 1.42 - 1.69 M_{\odot} ;

Clearly, RSVD is a better method in this case as it reduces computational costs by at least an order.

3. **Match Computation:** The above two factors proved RSVD to be a better method but there is another aspect that is really important to consider during analyses - *how much data is lost during dimension reduction?* If there is too much data loss, the method proves to be ineffective and can lead to the loss of important data points. In figures 2.5 and 2.6, we have computed the match between the original template matrix that SVD uses and the final reconstructed template matrix that RSVD returns.

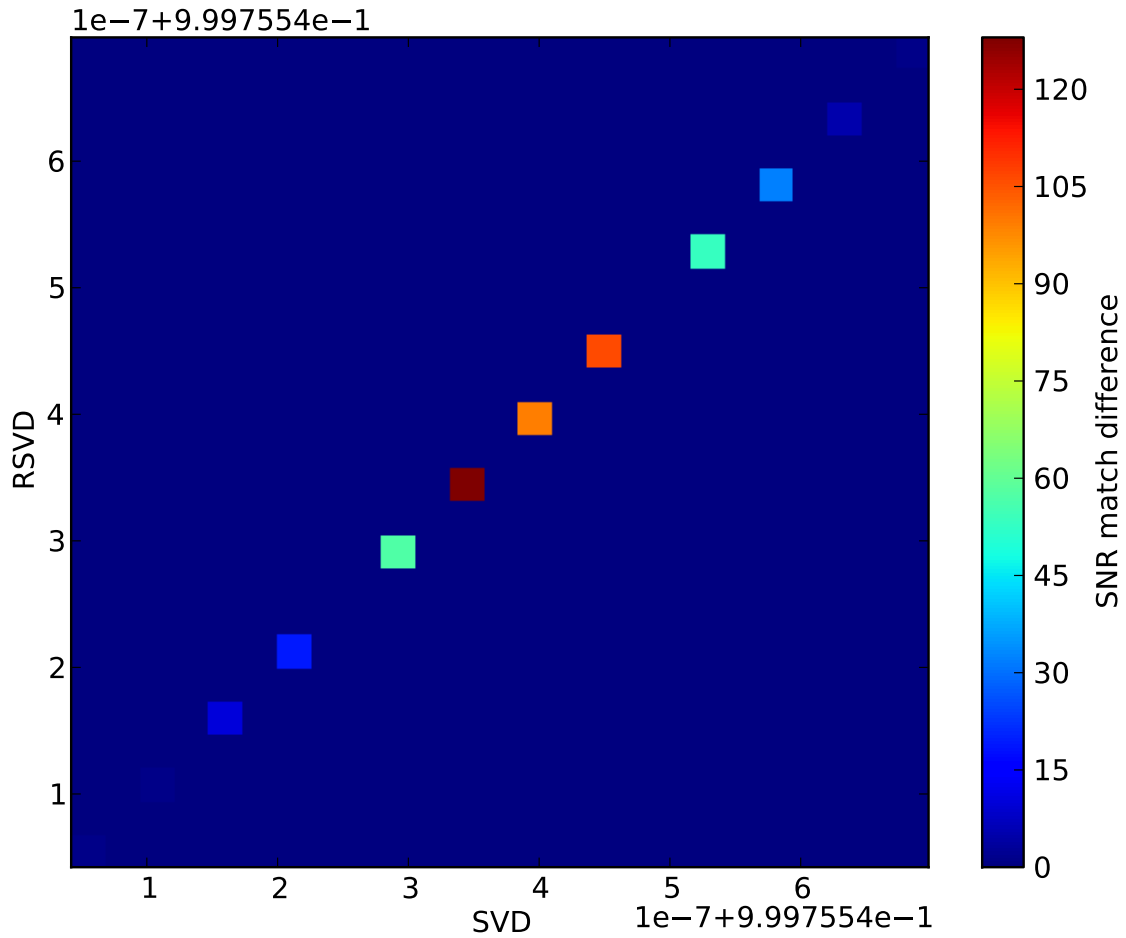


Figure 2.5: **SNR Match Computation:** The SNR match between the original template matrix that SVD uses and the reconstructed template matrix that RSVD returns after SNR reconstruction;

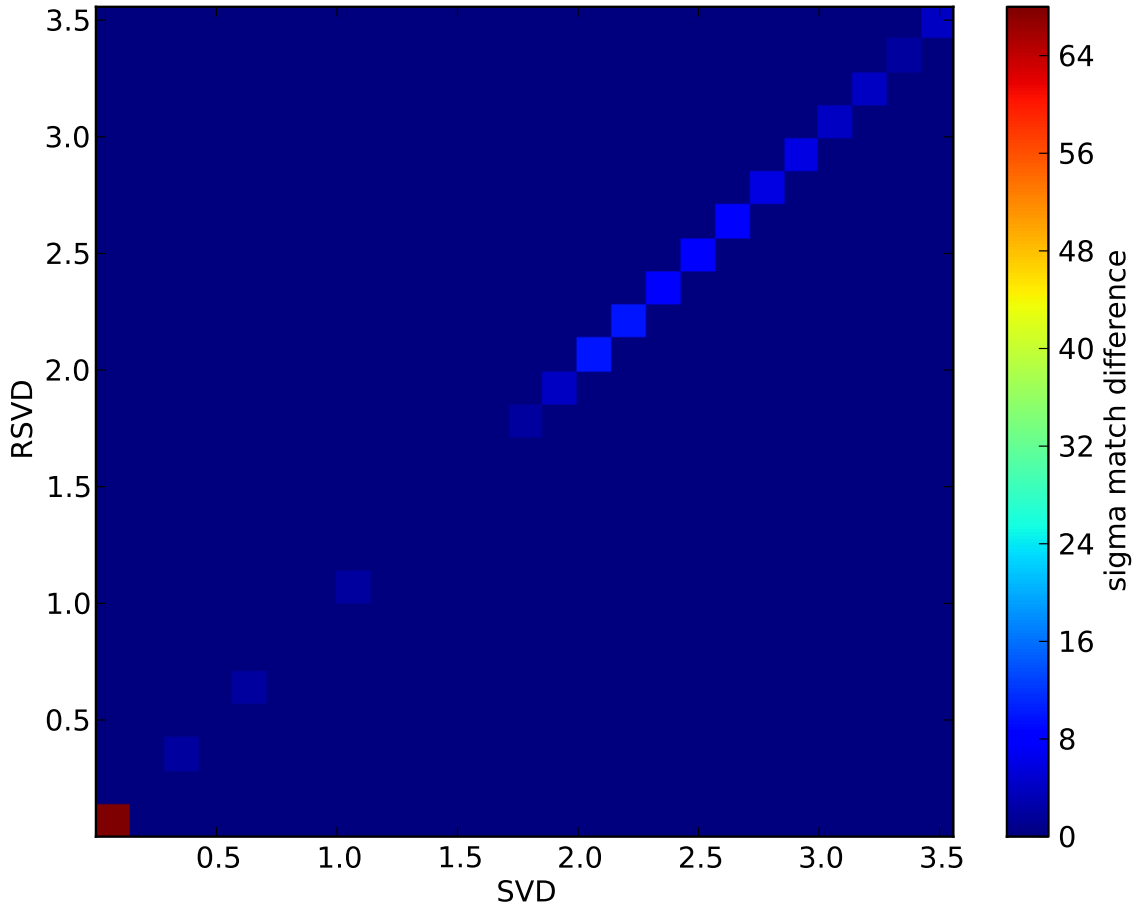


Figure 2.6: **Sigma Match Computation:** The calculated sigma values match computation between the original template matrix that SVD uses and the reconstructed template matrix that RSVD returns;

2.4 Discussion and Conclusion

Till date, there have been very few extensive analyses and studies about the sub-solar mass region owing to its complexity and computational costs. Notably, there have been dedicated GW searches for ultracompact objects in the sub-solar mass range ($0.2M_{\odot} - 1M_{\odot}$) using the data from the O1 [44] and O2 [45] runs. Both searches reported no significant candidates in this range. However, the null result can be used to constrain the merger rates and the abundance of sub-solar PBHs. In [46], the authors discuss improved detection methods by considering a specific model of PBH binary formation. One of the probable solutions that they suggest is altering the width of the frequency band that is considered for different mass bins, creating a more suitable template bank. Another more obvious solution is to improve

the PBH mass models that are currently being used in these analyses. The following chapter (3.1) extensively discusses PBH mass models, albeit in the super-solar mass region.

In [47], the authors consider both a monochromatic mass function and a model-independent approach for sub-solar mass PBHs and estimate their detectable limit while using LIGO, the Einstein Telescope (ET) and the Cosmic Explorer (CE). For PBHs with a monochromatic mass function, a detectable limit of PBHs is estimated. One of the major changes that they make while considering the model-independent approach, is to consider the merger of one sub-solar mass PBH with another larger super-solar mass PBH, which would result in a stronger signal. They finally predict that the abundance of PBHs in the mass range $0.2 - 1M_{\odot}$ can be constrained to an order of $\mathcal{O}(10^{-7})$ and $\mathcal{O}(10^{-8})$ for ET and CE respectively.

In this part of my thesis, we have considered and explored better data analysis techniques to cope with the various problems that arise during sub-solar mass searches. While considering the run-time and computational costs, **RSVD definitely performs better than SVD**. The match computation also shows that the data loss is minimal during dimension reduction. This leads us to conclude that RSVD will potentially perform better when it is introduced to larger template banks. It will help in conducting more complex analyses such as the subsolar searches for PBHs. In the super-solar mass range ($>1M_{\odot}$), it could also be used to include more parameters such as spin during CBC search analyses. This would be particularly useful in PBH analyses since they are predicted to have very low spins. Besides this, the next logical step would be to incorporate RSVD into the GstLAL search pipeline and use this new technique to rerun the O1, O2 and O3 sub-solar searches and also for future LVC chunk analyses.

**PART II: DISTINGUISHING PRIMORDIAL
BLACK HOLES FROM ASTROPHYSICAL
BLACK HOLES IN THE LOWER MASS GAP
REGION**

3.1 Introduction

The fluctuations in the early universe that arose naturally to produce primordial black holes (PBHs) are the same kind of fluctuations that are invoked to explain the formation of galaxies. This leads to an idea that PBHs exist over all mass ranges. [7] In the previous part, we looked at sub-solar mass primordial black holes - objects that would prove to be a "smoking gun" detection. But for a more conclusive approach towards the detection of these objects, we also need to consider other mass ranges. So in this part, we focus on super-solar mass PBHs and in particular, we focus on the lower mass gap region. The main problem with attempting to make a primordial binary black hole (PBBH) detection in this region is trying to differentiate it from an astrophysical binary black hole (ABBH). This is the main question we hope to answer in this part of the thesis. It is important to remember that the idea here is to set a basic framework for analysis, such that small tweaks can produce better and more accurate results in the future. I discuss these ideas in more detail in 3.5.

3.1.1 Studying the Lower Mass Gap Region

One of the many mysteries that baffle astronomers is the apparent mass gap between neutron star and black hole detections in the mass range 3 to 5 M_{\odot} range, illustrated in Fig. 3.1. While the highest observed NS mass is $2.14^{+0.20}_{-0.18}M_{\odot}$, theories predict that it can be higher. [48] These theories are based on various underlying assumptions which can only be validated by further observations. On the other hand, almost all detected BHs have a minimum component mass of $\sim 30 M_{\odot}$. Theoretical and observational arguments suggest that stellar evolution cannot produce BHs of mass lesser than $\sim 5 M_{\odot}$. [49] Both these facts lead to the potential existence of the lower mass gap. To be more comprehensive, we set our mass range between 3 M_{\odot} and 10 M_{\odot} throughout the analysis.

The lack of stellar evolution theory in this mass range supports the exploration of more exotic scenarios such as PBBHs. Further, as we previously discussed, PBBHs exist over all mass ranges. Both these facts, along with the general lack of detections motivate us to consider searching for PBBHs in the lower mass gap region as the searches would be less polluted in this region. Finally, there have been very few extensive studies about PBBHs in the mass gap regions which makes this a pioneering study.

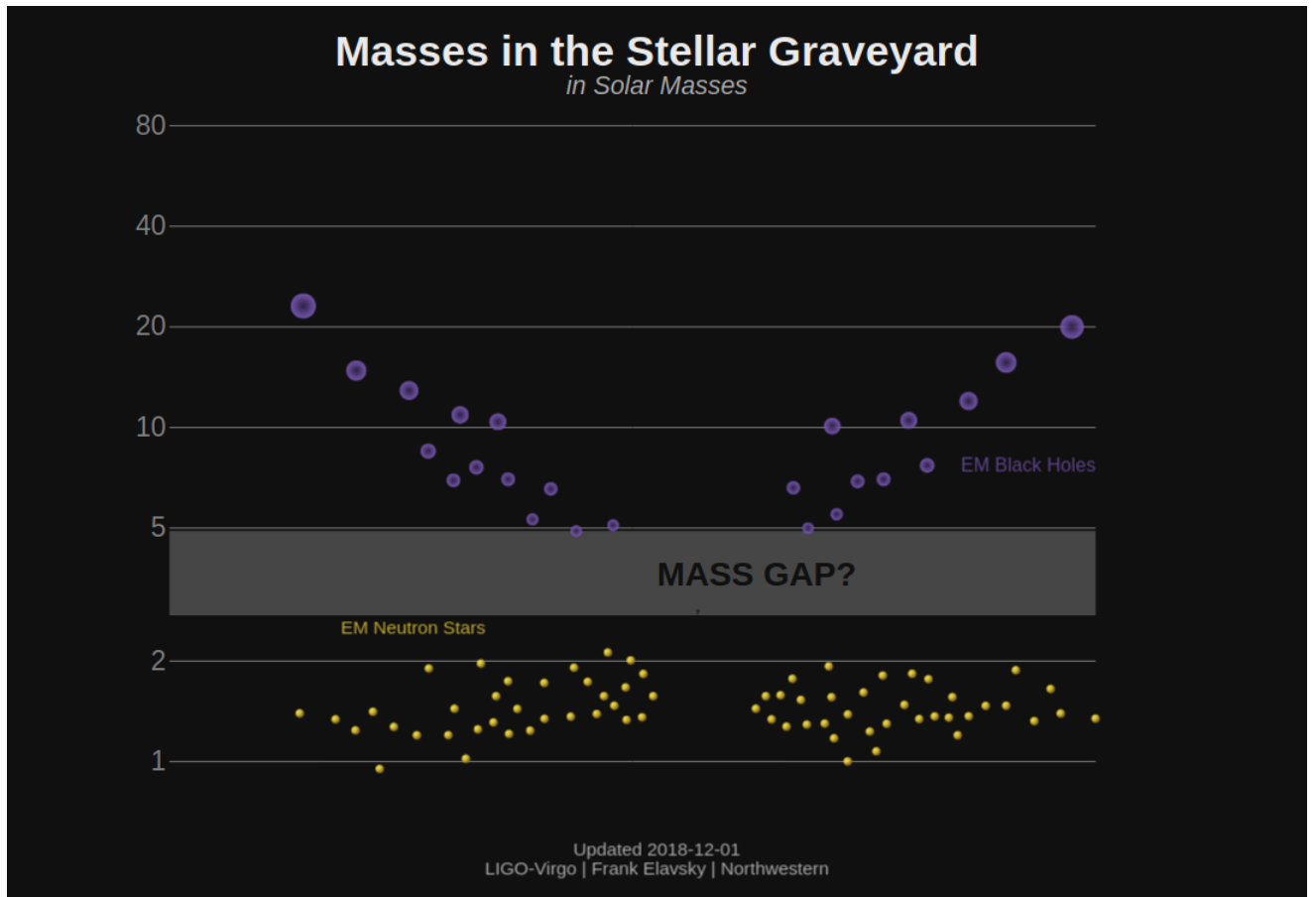


Figure 3.1: **Schematic Diagram** clearly showing the **Lower Mass Gap Region of $3\text{-}5 M_{\odot}$** , along with all the confident LIGO-Virgo Detections till date. [LIGO-Virgo/Frank Elavsky and Aaron Geller/Northwestern]

During the O3b run, two interesting events in the lower mass gap were detected - GW190425 and GW190814. **GW190425** is a compact binary system with a total mass of $3.5 M_{\odot}$ with component masses in the range 1.12 to $2.52 M_{\odot}$. [50] This observation is consistent with the inspiral of a BNS system although the total mass and chirp mass is larger than any known BNS system. To date, no electromagnetic or neutrino detections have been made in association with this event. The astrophysical implications are only speculative with a BNS merger being the most obvious and straightforward answer, however the lack of an electromagnetic counterpart does not help this theory. Another possibility is that this is a BH-NS merger system but this would also imply the existence of the BH in the mass gap region which is still a highly debatable topic since stellar evolution theory fails to predict BHs in this mass range. **GW190814** was perhaps an even more exciting detection because not only was it measured in the lower mass gap but it also has the most unequal mass ratio ever detected. [51] Additionally, the higher mass object is clearly a black hole at $23 M_{\odot}$ but the lower mass compact object of $2.6 M_{\odot}$ remains a complete mystery. In this case, there was also no successful electromagnetic follow-up. The authors conclude that the possibility of this kind of compact object arising from a NS-BH merger is low. This suggests the question - did LIGO/Virgo just detect the heaviest neutron star or the lightest black hole?

The discovery papers of both GW190425 [50] and GW190814 [51] mentions the possibility of these events being of exotic origin i.e. a primordial black hole. Naturally, for the purpose of this thesis, I would focus on this speculation. These two events have further motivated our study and also added to the relevance of it. The methods that we have developed here can be used to probe these events further. (refer section 3.5.3)

Current template banks that are used in LVC analyses are based on stellar models that have no predictions for the mass gap regions. This automatically means that they weigh the mass gap regions lesser. To fix this issue, we generate injections using specific models (refer section 3.3.1) in fixed mass ranges and input them into the detector at design sensitivity. We then use parameter estimation techniques to compute the posterior distributions of each model, while considering the models as our priors. In 3.2, I briefly discuss a few concepts of parameter estimation and Bayesian inference in gravitational-wave astronomy. If you are familiar with these concepts, you can skip ahead to the next section in which I discuss the methodology in further detail.

3.2 Parameter Estimation Primer

Bayesian inference and parameter estimation are the tools that help us make statements about the universe based on data. [2] In GW astronomy, it is used to retrace a detection back to its source and figure out various properties of the source. Essentially, Bayesian inference and PE form the language of GW astronomy. Parameter estimation, at the base level, deals with two main variables - θ and d . θ is the set of model gravitational-wave parameters while d is the data associated with measurement. Typically in PE estimation scenarios, there are four elements to consider - **the prior, the likelihood, the model evidence, and the posterior**.

With these elements, the main aim of Bayesian inference and our final goal is to construct a posterior distribution. This is a probability density function for θ given d . In simpler words, it helps us understand the relation between our chosen parameters and the actual data. This distribution finally helps us construct credible intervals for different parameters, such that we can estimate the value of a parameter confidently. For example, the component masses of the binary black hole event GW150914 were calculated using this method of credible interval construction. The **posterior distribution** is given by

$$p(\theta|d)$$

It is normalized such that

$$\int p(\theta|d)d\theta = 1 \quad (3.1)$$

But getting to this posterior distribution requires a few steps. According to Bayes theorem, the posterior distribution is given by

$$p(\theta|d) = \frac{\mathcal{L}(d|\theta)\pi(\theta)}{\mathcal{Z}} \quad (3.2)$$

where $\mathcal{L}(d|\theta)$ is the likelihood function of the data d given the parameters θ , $\pi(\theta)$ is the prior distribution of parameters and \mathcal{Z} is the evidence or normalization factor. We need to calculate or obtain each of these terms to calculate the posterior distribution.

The **likelihood function** $\mathcal{L}(d|\theta)$ includes both the detector noise and the gravitational wave signal and is a description of measurement. It essentially answers the question - "How likely is it for a gravitational wave to be in the data?". It does not directly depend on the population we're choosing so for the purpose of this analysis, it does not matter too much. However, for gravitational-wave astronomy, a Gaussian-noise likelihood function is typically assumed.

The **prior** $\pi(\theta)$ is also something we choose. This element contains the information that we already know, before carrying out any measurements. Any prior knowledge that we have about any parameter(s) is encoded here. This is an important aspect for this analysis, I will discuss this in more detail as we proceed.

Using the gravitational-wave Bayesian inference library BILBY, we obtain the final element - the **evidence** \mathcal{Z} or the normalization factor, which is given by:

$$\mathcal{Z} = \int \mathcal{L}(d|\theta)\pi(\theta)d\theta \quad (3.3)$$

Practically, the evidence is a single number which, when compared with another evidence, becomes very useful. It is the completely marginalized likelihood function. But an important aspect is that the evidence is used to do model selection. It can be used to answer the question "which model is statistically preferred by the data and by how much?". This will also be of key importance to reach a conclusion for our analysis.

A summary of the various elements of parameter estimation and Bayesian inference is listed below:

Parameter Estimation Elements		
Notation	Element Name	
θ	Model Parameters	GW Parameters
d	Data	Associated with measurement
$\pi(\theta)$	Prior Distribution	Prior Knowledge
$\mathcal{L}(d \theta)$	Likelihood Data	Based on Noise Models & GW waveforms
$P(\theta d)$	Posterior Distribution	Posterior knowledge obtained using BILBY
\mathcal{Z}	Evidence/Normalization Factor	"how likely is it that the model is correct?"

3.2.1 BILBY: The Tool

The primary tool used for parameter estimation of gravitational waves by the LIGO-Virgo Collaboration is LALInference [52]. This was the very first tool that was developed for analyses during the O1 and O2 runs. In 2018, a simpler and more user-friendly package was developed called BILBY [53]. This open-source software is now broadly used across the collaboration and outside. This package also allows beginners to access expert-level infrastructure. A simple example run is capable of producing the probability distributions of the various parameters. The main difference between the two packages is the modularity and the adaptability. As already mentioned in the previous sections, BILBY is what we will use for our parameter estimation analysis.

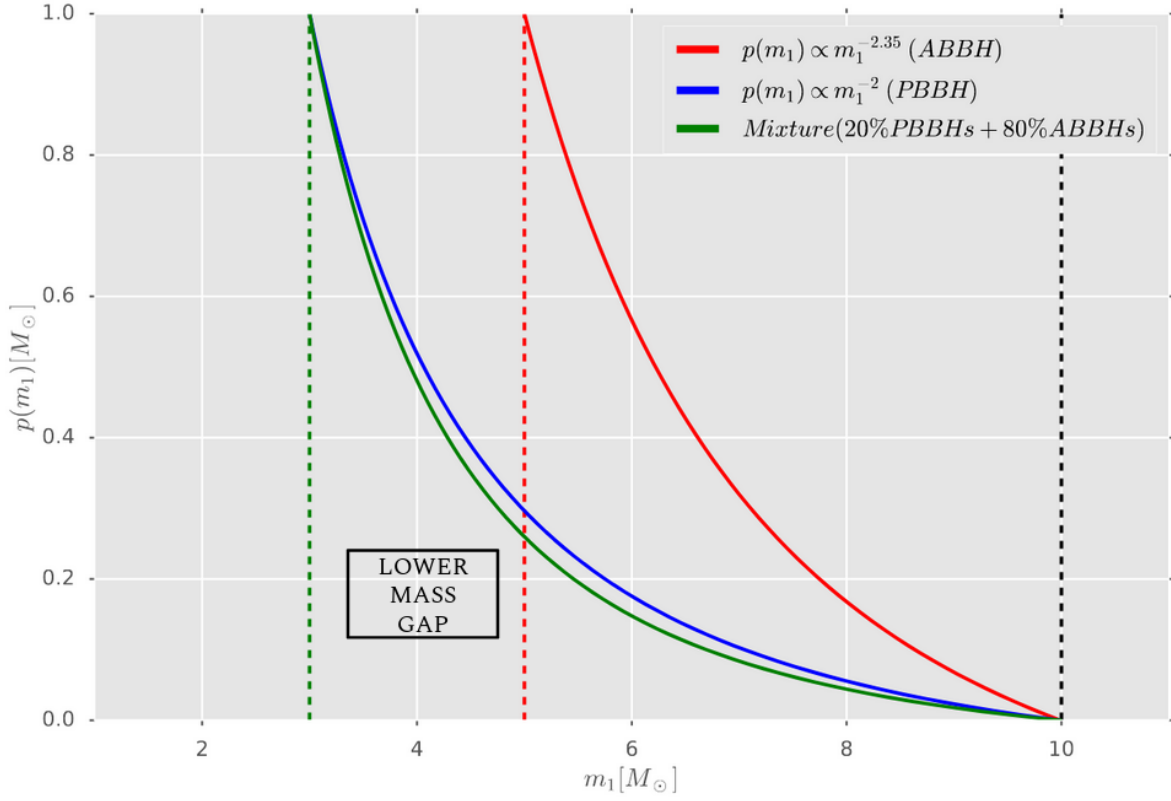


Figure 3.2: **Power-Law Mass Distributions for ABBHs and PBBHs:** an example plot showing the nature of the prior distributions; the red, blue and green lines represent the ABBH (3.4), PBBH (3.8) and mixture (Mix_M2) populations respectively; the vertical dashed lines enclose the mass ranges of each and also the lower mass gap region;

3.3 Methodology

3.3.1 Model Selection

One of the most important steps of this analysis was choosing appropriate models to shape our data - these models essentially form the basis of our entire study. However, once we set up the basic framework, adding and changing models is a simple step. Thus, for a preliminary analysis, we chose to proceed with the power-law mass model for both ABBHs and PBBHs.

Astrophysical Binary Black Holes (ABBHs)

A power-law distribution for the primary mass m_1 is assumed as the canonical distribution for ABBHs.

$$\begin{aligned} p(m_1) &\propto m_1^{-\alpha}, \\ \text{or} \\ \pi(m_1 | \alpha, m_{min}, m_{max}) &\propto m_1^{-\alpha}. \end{aligned} \tag{3.4}$$

This can also be written as

$$p(m_2 | m_1) = \frac{1}{m_1 - M_{min}}, \tag{3.5}$$

with $M_{min} \leq m_2 \leq m_1$ and $m_1 + m_2 \leq 100M_\odot$. A uniform distribution on the secondary mass m_2 is assumed where the mass range is between $M_{min} = 5M_\odot$ and m_1 . All masses are taken to be source-frame masses. Following eqn. 3.5, a joint population distribution on m_1 and m_2 can be written as

$$p(m_1, m_2 | \alpha) \propto \frac{m_1^{-\alpha}}{m_1 - M_{min}}. \tag{3.6}$$

In previous papers [54] [55], $\alpha = 2.35$ is used. The value of α is determined from hierarchical analyses and at the 90% credible interval, it is found to be

$$\alpha = 2.5_{-1.6}^{+1.5}. \tag{3.7}$$

It is important to note that the power-law is dependent on many arbitrary assumptions such as a flat distribution in the mass ratio, redshift-independent merger rate and mass distribution. Additionally, the lower mass cut-off M_{min} plays a direct role in contributing to the shape of the power law.

Primordial Binary Black Holes (PBBHs)

In the case of PBBHs, we consider a power law that takes the form:

$$p(m_1) \propto m_1^{\gamma-1} \text{ where } \gamma = \alpha + 1. \quad (3.8)$$

According to [7], the PBH spectrum would look like this if the early universe consisted of small density fluctuations superposed on a Friedmann background. This kind of model arises naturally if the PBHs form from the scale-invariant density perturbations or from other mechanisms such as the collapse of cosmic strings. With this kind of model, the PBH mass spectrum depends on two things - the **equation of state** w and the **nature of the initial density fluctuations**. The equation of state determines how big a region must be when it stops expanding in order to collapse against the pressure forces and produce a PBH. It is dependent on the pressure p and energy density ρ at that point in the universe as $w \equiv p/\rho$. On the other hand, the nature of density fluctuations determines how likely a region is to stop expanding when it has reached the size determined by w .

The relation between γ and the equation of state w is given by:

$$\gamma = \alpha + 1 = -\frac{2w}{1+w}; \quad \gamma = \begin{cases} \gamma \neq 0, & m_{min} \ll m_{max} \\ \gamma = 0, & m_{min} < m_1 < m_{max} \end{cases} \quad (3.9)$$

To understand how the value of w and subsequently α affects our analysis, we need to take a better look at the FLRW (*Friedmann-Lemaître-Robertson-Walker*) equations. When the equation of state w is used in these equations, it describes the evolution of a homogeneous and isotropic universe as a perfect cosmological fluid. The solutions scale as follows, each describing the contribution of different sources to the pressure p :

$$\rho \propto a^{-3(1+w)} = \begin{cases} w = 0 \text{ (matter)} \\ w = -\frac{1}{3} \text{ (radiation)} \\ w = 1 \text{ (vacuum)}, \end{cases} \quad (3.10)$$

where a is the scale factor.

Further, we specifically want to consider the non-inflationary case since PBHs did not form *during* inflation but rather, *after* inflation. This means that we can consider our search for PBHs from the radiation-dominated era of the universe and set the lower boundary value as $w = -1/3$. Since we expect PBHs to have traveled through the universe and into the present era, we set our upper boundary limit as $w = 1$. In a non-inflationary scenario, the condition then becomes

$$w \in \left(-\frac{1}{3}, 1\right) \implies \gamma \in (-1, 1) \implies \boxed{\alpha \in (0, -2)} \quad (3.11)$$

For the purpose of our analysis, this is the range of α we consider to simulate our populations.

3.3.2 Mock Populations and Injections

In the previous section, I discussed the power-law models that we are considering. The next step would be to choose what we want our population to look like i.e. what percentage of ABBHs and PBBHs do we choose? This basically means that we are populating the lower mass gap region with a mix of ABBHs and PBBHs. Once we have decided what we want our population to look like, we can generate injections using existing LVC code. For our case, we chose a 80-20 ratio in favour of ABBHs. This is an arbitrary choice and different ratios can be considered in the future. Fig. 3.3 (detector mass) and Fig. 3.4 (source mass) describe the mass range of the three scenarios.

We consider three different scenarios for our analyses:

Three Scenarios					
Model Name	Scenario	Mass Range of ABBHs M_{\odot}	α	Mass Range of PBBHs M_{\odot}	α
Astro	100% ABBHs	5 - 10	2.35	-	-
Mix_0	80% ABBHs + 20% PBBHs	5 - 10	2.35	3 - 10	0
Mix_M2	80% ABBHs + 20% PBBHs	5 - 10	2.35	3 - 10	-2

3.3.3 Parameter Estimation Techniques

Solving the Evidence with BILBY

In our case, the prior $\pi(\theta)$ is simply the mass model we have chosen for the analysis and no other parameter. Since it depends on our existing knowledge, it changes for the different models and scenarios. In our case, we consider both ABBH and PBBH populations in the lower mass gap. This means that there are two different priors - $\pi_{ABBH}(\theta)$ and $\pi_{PBBH}(\theta)$ that we need to consider. Consequently, their respective evidences can be written as

$$\mathcal{Z}_{ABBH} = \int \mathcal{L}(d|\theta) \pi_{ABBH}(\theta) d\theta, \quad (3.12)$$

and

$$\mathcal{Z}_{PBBH} = \int \mathcal{L}(d|\theta) \pi_{PBBH}(\theta) d\theta. \quad (3.13)$$

The Bayes factor $\mathcal{B}_{ABBH}^{PBBH}$ then answers which of these priors is correct for the population we're considering, depending on how large or small the value is. Computing the Bayes factor for each scenario is our final goal as it directly answers the question "which model is more likely".

$$\mathcal{B}_{ABBH}^{PBBH} = \frac{\mathcal{Z}_{PBBH}}{\mathcal{Z}_{ABBH}}. \quad (3.14)$$

However, the main issue in this case is that the BILBY run will only evaluate

$$\mathcal{Z} = \int \mathcal{L}(d|\theta) \pi(\theta) d\theta, \quad (3.15)$$

which is different from what we want since $\pi(\theta) \neq \pi_{ABBH}(\theta) \neq \pi_{PBBH}(\theta)$.

One way around this problem is to redo the BILBY runs to get the different evidences but this would be both time-consuming and also a waste of computational resources. Instead we can change the form of the evidence to compute the required evidence values:

$$\begin{aligned} \mathcal{Z}_{PBBH} &= \int \mathcal{L}(\theta) \pi_{PBBH}(\theta) d\theta \\ &= \int \mathcal{L}(\theta) \pi(\theta) \frac{\pi_{PBBH}(\theta)}{\pi(\theta)} d\theta \\ &= \mathcal{Z} \int \pi(\theta|d) \frac{\pi_{PBBH}(\theta)}{\pi(\theta)} d\theta \\ &= \mathcal{Z} \left\langle \frac{\pi_{PBBH}(\theta)}{\pi(\theta)} \right\rangle_{\pi(\theta|d)}. \end{aligned} \quad (3.16)$$

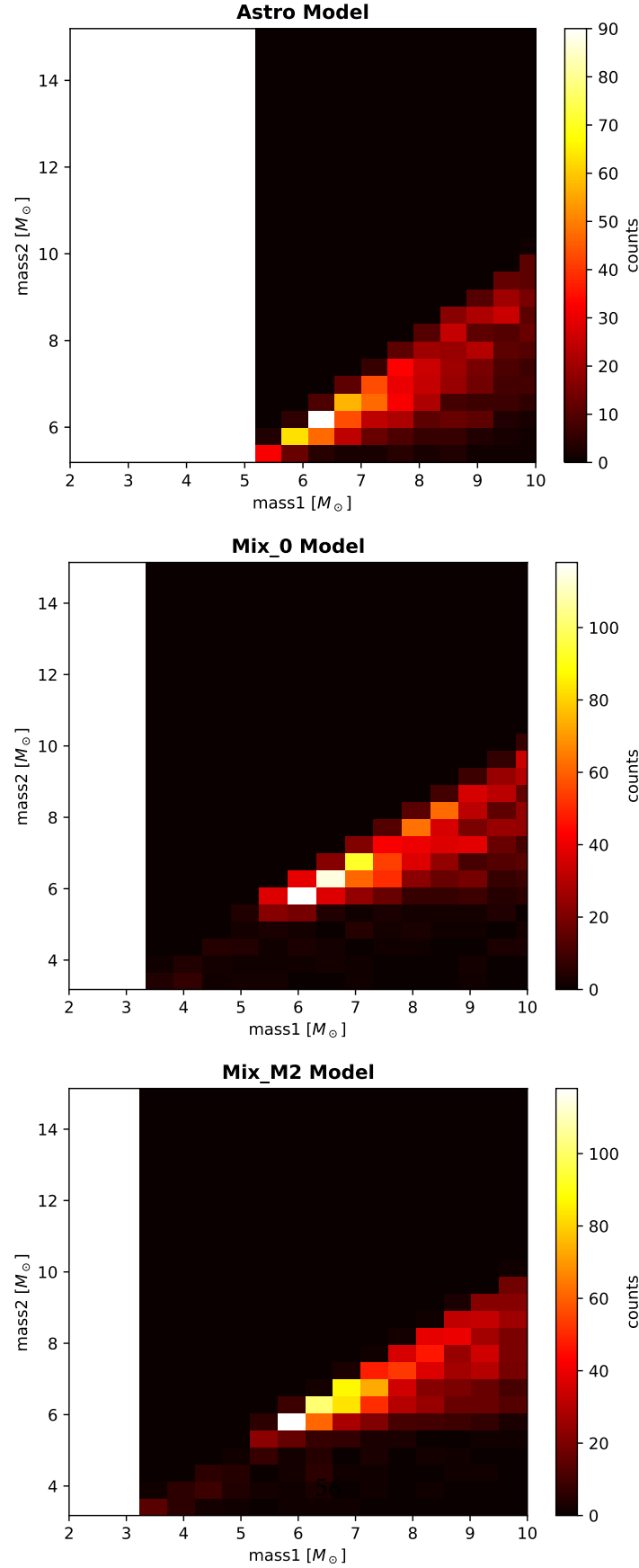


Figure 3.3: **Gravitational Wave Simulations for the Three Scenarios (redshifted values):** mass parameters m_1 and m_2 for the three models; the mass parameter values are slightly higher, due to redshift;

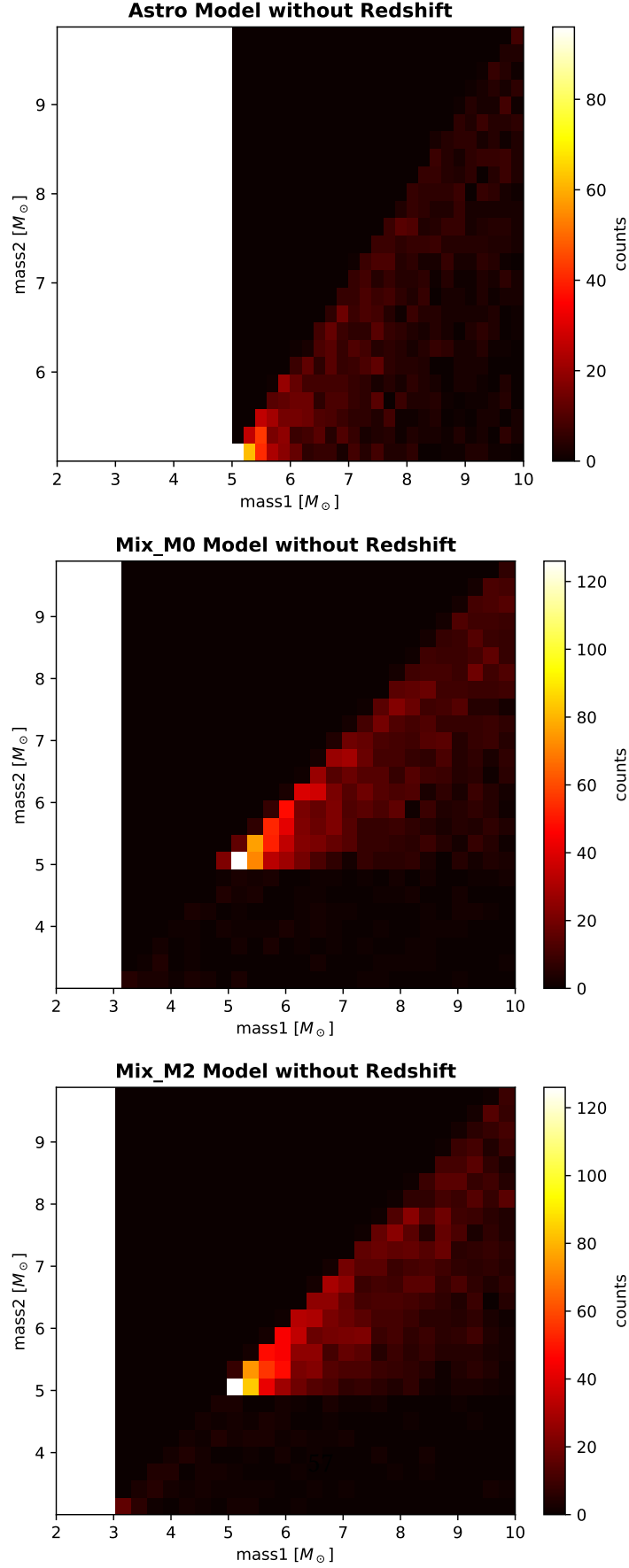


Figure 3.4: **Gravitational Wave Simulations for the Three Scenarios (redshift-corrected values):** mass parameters m_1 and m_2 for the three models;

In the second last line, we use Bayes theorem to calculate the posterior of the measurement i.e. what we know about the gravitational-wave parameters after the measurement which also includes the detector data d . The posterior $\pi(\theta|d)$ is given by the BILBY run. In the last line, we solve the integral by *importance sampling* the posterior.

Similarly, we have an expression for the ABBH evidence:

$$\mathcal{Z}_{ABBH} = \mathcal{Z} \left\langle \frac{\pi_{ABBH}(\theta)}{\pi(\theta)} \right\rangle_{\pi(\theta|d)}. \quad (3.17)$$

Calculating the Priors

In our analysis, our only prior is the model with one mass parameter that we choose to describe our population. This means that we have three different priors $\pi(\theta)$ for the three different scenarios we consider. Since we are only focusing on only the primary mass m_1 for now, $\theta = m_1$.

1. **100% ABBHs:** The Astro model is the simplest scenario out of the three, the prior becomes:

$$\pi_{ABBH}(m_1) = C_{ABBH} m_1^{-2.35}, \quad (3.18)$$

where $5M_\odot < m_1 < 10M_\odot$ and C_{ABBH} is the normalization constant given by:

$$C_{ABBH} = \frac{1}{\int_5^{10} m_1^{-2.35} dm_1}. \quad (3.19)$$

Thus, the final expression is:

$$\boxed{\pi_{ABBH}(m_1) = \frac{1}{\int_5^{10} m_1^{-2.35} dm_1} m_1^{-2.35}}. \quad (3.20)$$

2. **80% ABBHs + 20% PBBHs (Mixed Models):** Once we start considering a mixed model of two different populations, we need to take into account the following: the different power-law indices α , the different mass ranges and also the parameter f of either population. f describes how often we draw an injection from either population during the analysis. A small value of f is chosen for the events that are expected to be lower in number. This also means that for a more thorough analysis, we need to consider more injections for these cases. Since PBBH detections are assumed to be small in number when compared to ABBH detections, we consider $f = 0.2$ for it. While this choice is relatively arbitrary, it is possible to determine a more accurate value from the amplitude of the joint distribution of ABBHs and PBBHs.

Mix_0 Model: In this case, the evidence can be written as:

$$\begin{aligned}\pi_{PBBH}^{Mix_0}(m_1) &= \pi_{ABBH+Mix_0} \\ &= C_{ABBH} m_1^{-2.35} + C_{PBBH} m_1^0,\end{aligned}\quad (3.21)$$

where $3M_\odot < m_1 < 10M_\odot$. The normalization constant C_{PBBH} in this scenario is given by:

$$C_{PBBH} = \frac{f}{\int_3^{10} m_1^0 dm_1} m_1^0. \quad (3.22)$$

This finally gives us the expression for the prior:

$$\pi_{PBBH}^{Mix_0}(m_1) = \frac{1-f}{\int_5^{10} m_1^{-2.35} dm_1} m_1^{-2.35} + \frac{f}{\int_3^{10} m_1^0 dm_1} m_1^0. \quad (3.23)$$

Mix_M2 Model: Similarly, for the third scenario or Mix_M2 Model, we have:

$$\begin{aligned}\pi_{PBBH}^{Mix_M2}(m_1) &= \pi_{ABBH+Mix_M2} \\ &= C_{ABBH} m_1^{-2.35} + C_{PBBH} m_1^{-2}.\end{aligned}\quad (3.24)$$

where $3M_\odot < m_1 < 10M_\odot$. The normalization constant C_{PBBH} changes accordingly to be:

$$C_{PBBH} = \frac{f}{\int_3^{10} m_1^{-2} dm_1} m_1^{-2}. \quad (3.25)$$

Thus, we finally have the prior expression as:

$$\pi_{PBBH}^{Mix_M2}(m_1) = \frac{1-f}{\int_5^{10} m_1^{-2.35} dm_1} m_1^{-2.35} + \frac{f}{\int_3^{10} m_1^{-2} dm_1} m_1^{-2}. \quad (3.26)$$

Combining the Evidences

Now that we have derived expressions for the evidence of one injection (3.17, 3.16) and the prior calculations (3.20, 3.23, 3.26), the next step would be to combine the evidences of all the injections. Doing this would help us calculate the Bayes factor (3.6) and subsequently help us arrive at an answer to our final question - which population model is more likely in this region?

If we consider N events, the combined evidence is simply calculated by taking the product over all the events, assuming that selection effects are not significant (we discuss how to treat

the selection effect below in section 3.3.3). Following equations 3.16 and 3.17, we can write the general expressions as:

$$\mathcal{Z}_{PBBH} = \prod_{i=1}^N \mathcal{Z}^i \left\langle \frac{\pi_{PBBH}(\theta)}{\pi(\theta)} \right\rangle_{\pi(\theta|d_i)}, \quad (3.27)$$

and

$$\mathcal{Z}_{ABBH} = \prod_{i=1}^N \mathcal{Z}^i \left\langle \frac{\pi_{ABBH}(\theta)}{\pi(\theta)} \right\rangle_{\pi(\theta|d_i)}. \quad (3.28)$$

The only change with respect to the individual evidences is that we are now importance sampling the posterior of the i th event $p(m_1|d_i)$. Further, we have two prior expressions for \mathcal{Z}_{PBBH} :

$$\mathcal{Z}_{PBBH}^{Mix_0} = \prod_{i=1}^N \mathcal{Z}^i \left\langle \frac{\pi_{PBBH}^{Mix_0}(\theta)}{\pi(\theta)} \right\rangle_{\pi(\theta|d_i)}, \quad (3.29)$$

and

$$\mathcal{Z}_{PBBH}^{Mix_M2} = \prod_{i=1}^N \mathcal{Z}^i \left\langle \frac{\pi_{PBBH}^{Mix_M2}(\theta)}{\pi(\theta)} \right\rangle_{\pi(\theta|d_i)}. \quad (3.30)$$

Bayesian Model Selection (Computing the Bayes Factor)

Now that we have the final combined evidences, we can compute the combined Bayes factor $\mathcal{B}_{ABBH}^{PBBH}$ for each scenario and conclusively reach an answer to our question. For the Astro Model, the Bayes factor is computed with respect to the evidence of the waveform model used. Since this scenario consists of no PBBHs, we expect the Bayes factor $\mathcal{B}_{ABBH}^{PBBH}$ to favour the astrophysical population of ABHs.

For Models Mix_0 and Mix_M2, the expressions for the combined evidences (3.29 and 3.30) are used to get the general expression:

$$\mathcal{B}_{ABBH}^{PBBH} = \frac{\mathcal{Z}_{PBBH}}{\mathcal{Z}_{ABBH}} = \prod_{i=1}^N \frac{\left\langle \frac{\pi_{PBBH}(\theta)}{\pi(\theta)} \right\rangle_{\pi(\theta|d_i)}}{\left\langle \frac{\pi_{ABBH}(\theta)}{\pi(\theta)} \right\rangle_{\pi(\theta|d_i)}}; \quad (3.31)$$

where $\pi_{PBBH}(\theta)$ can be either $\pi_{PBBH}^{Mix_0}(\theta)$ (3.23) or $\pi_{PBBH}^{Mix_M2}(\theta)$ (3.26).

Selection Effects

So far, we have dealt with big chunks of data in the form of injection sets which makes some of the events more detectable than others. We can account for these internal selection effects by including an extra term in the expression for evidence:

$$\mathcal{Z}_{ABBH} = \prod_{i=1}^N \mathcal{Z}^i \frac{1}{\alpha_{ABBH}} \left\langle \frac{\pi_{ABBH}(\theta)}{\pi(\theta)} \right\rangle_{\pi(\theta|d_i)}, \quad (3.32)$$

where

$$\alpha_{ABBH} = \int p(\text{det}|\vec{\theta}) p(\vec{\theta}|\mathcal{H}_{ABBH}) d\vec{\theta}. \quad (3.33)$$

Similarly for PBBHs, we have:

$$\mathcal{Z}_{PBBH} = \prod_{i=1}^N \mathcal{Z}^i \frac{1}{\alpha_{PBBH}} \left\langle \frac{\pi_{PBBH}(\theta)}{\pi(\theta)} \right\rangle_{\pi(\theta|d_i)}, \quad (3.34)$$

where

$$\alpha_{PBBH} = \int p(\text{det}|\vec{\theta}) p(\vec{\theta}|\mathcal{H}_{PBBH}) d\vec{\theta}. \quad (3.35)$$

The Bayes factor consequently changes to be:

$$\mathcal{B}_{ABBH}^{PBBH} = \frac{\mathcal{Z}_{PBBH}}{\mathcal{Z}_{ABBH}} = \prod_{i=1}^N \frac{\alpha_{ABBH}}{\alpha_{PBBH}} \frac{\left\langle \frac{\pi_{PBBH}(\theta)}{\pi(\theta)} \right\rangle_{\pi(\theta|d_i)}}{\left\langle \frac{\pi_{ABBH}(\theta)}{\pi(\theta)} \right\rangle_{\pi(\theta|d_i)}} \quad (3.36)$$

where $\pi_{PBBH}(\theta)$ can be either $\pi_{PBBH}^{Mix_0}(\theta)$ or $\pi_{PBBH}^{Mix_M^2}(\theta)$.

3.4 Results and Discussion

The main goal of this work was to answer the question - *"How many gravitational wave detections do we need before we can distinguish a purely astrophysical population from a mixture population of astrophysical and primordial black holes in the lower mass gap region?"* To do this, we first studied models that describe the lower mass gap region. Using these models, we generated injections or "fake GW signals" and injected the detectors with them at design sensitivity. We used a total of 4266 injections, in the range of 3-10 M_{\odot} : 1778 from the astrophysical population and 2488 from the primordial black hole population. We then used Bayesian inference techniques to estimate the parameters and finally calculated the corresponding Bayes factor. This factor basically gives us the information about which model is

more likely to describe a population in a given mass range for a fixed number of detections. It is natural to assume that if we increase the number of detections, the Bayes factor value will also correspondingly change.

Ultimately, the main challenge to overcome with this kind of analysis is the long run-times and the high computational costs. This stems from the fact that we are considering low masses and subsequently, we are dealing with very long waveforms. Keeping this in mind, the following caveats need to be considered while evaluating our final result:

1. We chose very simple power-law distribution mass models to set up the framework of this kind of analysis so it does not accurately portray the exact nature of this mass region. For more precise results or rather, for a better answer to our initial question, we need to consider other complicated models that take into account various features predicted by early universe cosmologists. (discussed in more detail in 3.5.1)
2. Our analysis does not take into account any of the internal selection effects that we discussed above in section 3.3.3. Taking the selection effect parameters α_{ABBH} and α_{PBBH} occasionally (and not always) significantly alters the final Bayes factor value. Hence, for greater accuracy, we need to take that into account. In the future, this can be retrieved by using the GWDET package. ¹.
3. We chose the relative percentages of ABBHs to PBBHs as 80%:20%. This choice was arbitrary with the assumption that PBBHs are relatively rarer than ABBHs. The fact that PBBHs are lower in number might directly contribute to the result. Effectively, this means that if we were to choose a different ratio with higher number of PBBHs, distinguishing between the two populations might be easier. In this case, about 3% (or 75) of all the primordial black hole injections were placed in the lower mass gap region as shown in Fig.3.5. In the future, we will try to motivate these percentages better by consulting black hole population synthesis communities.
4. Due to some unforeseen delays caused by cluster issues and the subsequent lack of time, we could not evaluate the Mix_0 Model entirely and hence, it has been omitted from this section entirely.

In our case, preliminary results (Fig. 3.6) show that neither the ABBH nor the ABBHPBBH mixture populations favour the Mix_M2 model. We were expecting the ABBHPBBH mixture population to favour the Mix_M2 model. Therefore, we suspect there are some issues with properly modeling this mixture population. We attribute this to the internal selection effects and possibly other effects that we are investigating.

¹<https://github.com/dgerosa/gwdet>

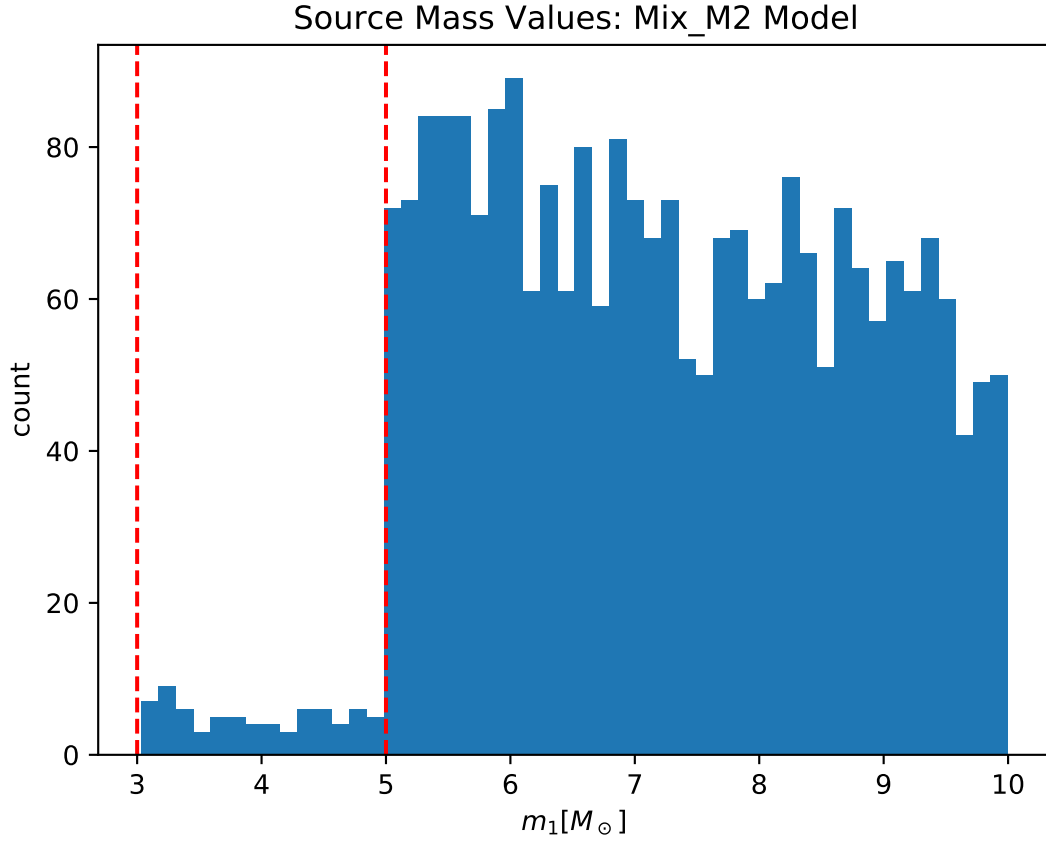


Figure 3.5: **Source Mass Values of the Mix_M2 Model:** the red lines indicate the lower mass gap region; 75 injections (out of 2488) from the primordial black hole Mix_M2 population were placed in this region;

An additional goal of this work was to set up a framework for future improved analyses which we have succeeded in doing. Any similar analysis after this would only require some simple changes - mainly in the model selection step, making it very effortless and straightforward. The simple power-law distribution model [7] that we chose gave us substantial results, enough to form an approximate idea about the lower mass gap region. However, next, we would like to explore models that take into account the thermal history of the universe [21] for a more accurate result. The method that we have discussed and followed here can be applied to both simulated and real detections. As a further step, after determining the best model, we can also replace the simulated data with real data from the observing runs O1, O2 and O3.

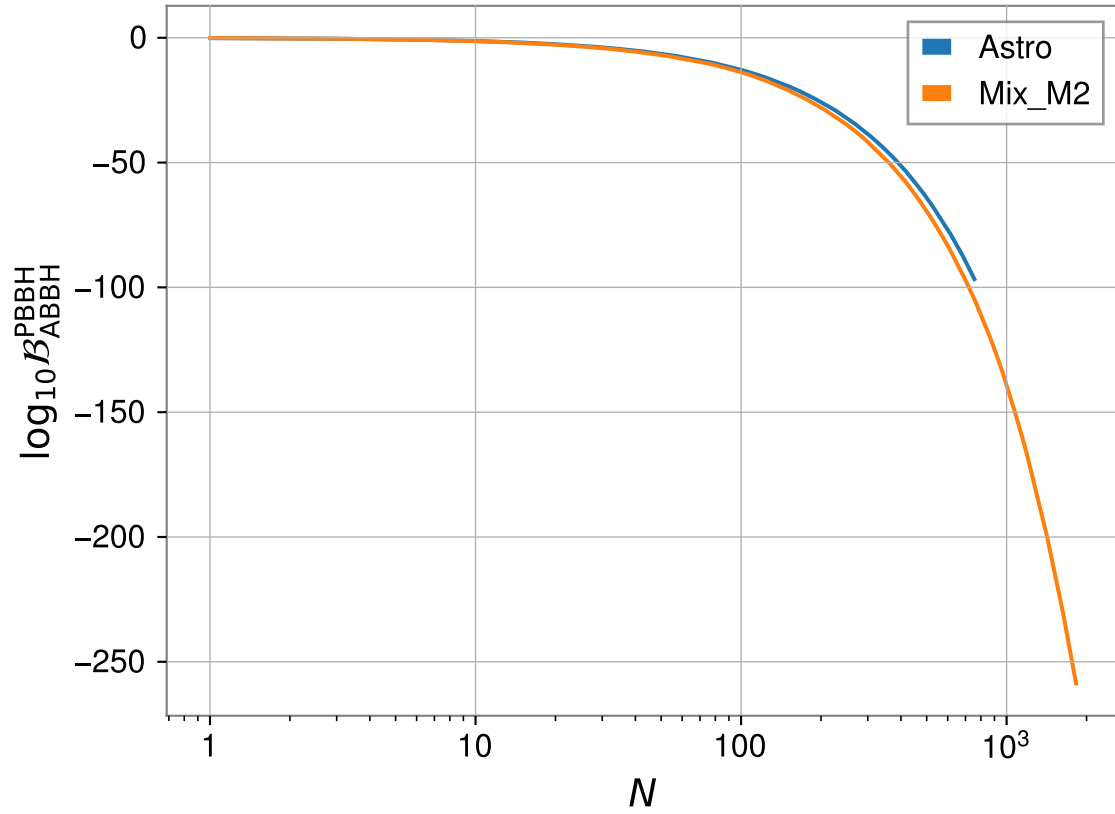


Figure 3.6: **Bayes Factor Plot:** Bayes factor value calculated for each injection where N is the injection count/number; this plot should be considered

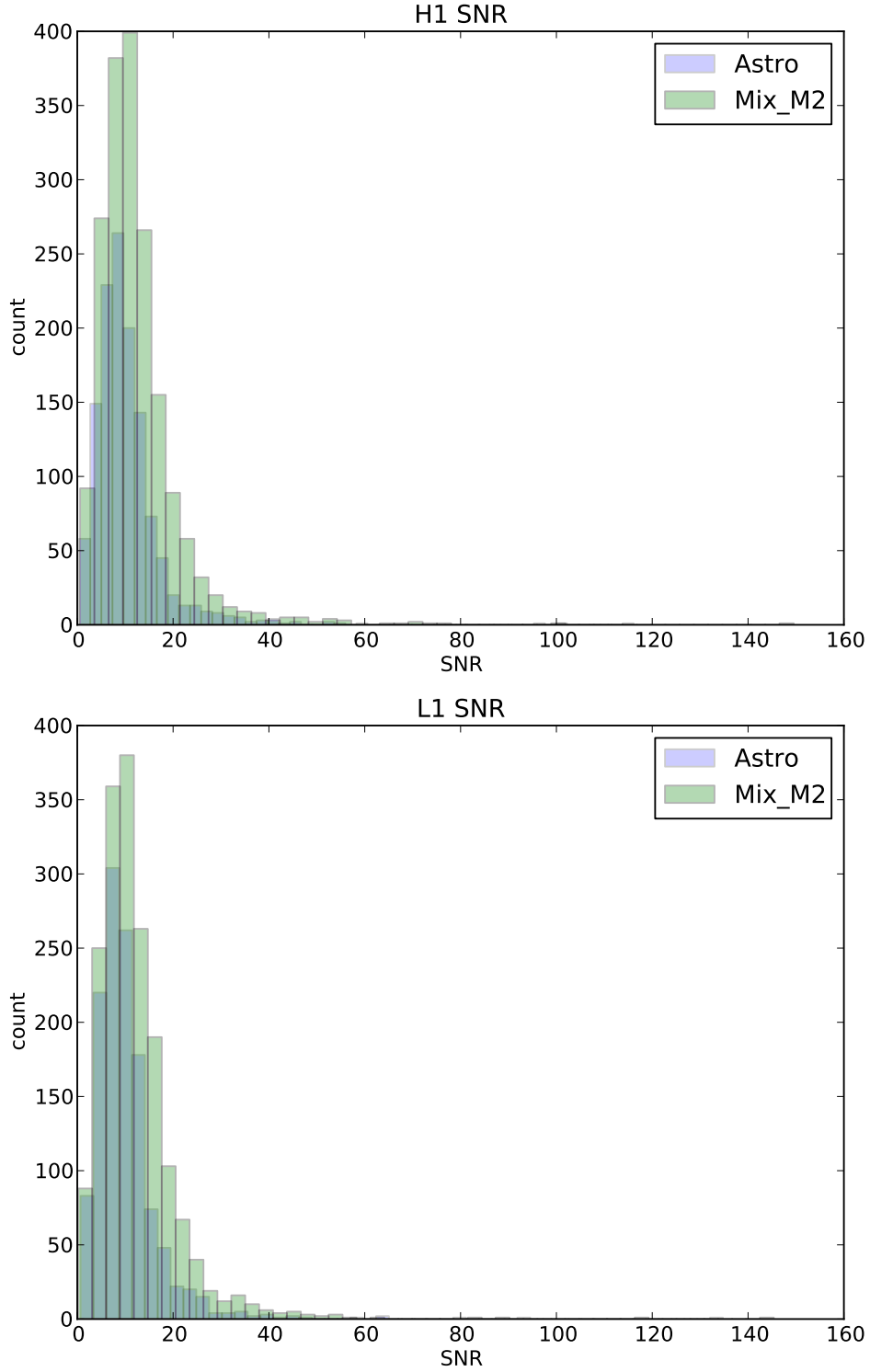


Figure 3.7: **H1/L1 Network SNR:** plots showing the SNR values for the GW injections or "fake-signals" at the Hanford (H1) and Livingston (L1) detectors; the network SNR values are a good approximation of the real detections since it takes into account the Gaussian noise;

3.5 Future Projects

One of the most interesting parts of this project was discussing the many ideas that we had over time and subsequently discovering the scope of many follow-up projects. The layout of this analysis can be used, with various tweaks and additions, for these projects. This would possibly lead to better and more accurate results of both this study and other related studies. I discuss most of the ideas that we have had in this section, including the ones we intend to work on in the next several months.

3.5.1 Addition of Models

Undeniably, the first thing that comes to mind, as previously mentioned, is to include more models. The power-law distribution is a rudimentary model and has helped us gain an idea of what to expect from an analysis of this nature. However, to get a more comprehensive result, we need to consider more models and specifically, PBBH-specific models. It would also be sensible to focus on models consisting of parameters such as spin, redshift, chirp mass, eccentricity, etc. While this would give us a good lead, the study would be the most thoroughgoing if we considered a model of mixed parameters. This is because every parameter is linked to each other in one way or another and the analysis will remain incomprehensive if we ignore these dependencies.

Models Based on the Mass Parameter ²

The general mass function of PBHs, over all mass ranges, can be written as

$$\psi(M) \propto M \frac{dn}{dM}, \quad (3.37)$$

where dn is the number density of PBHs in the mass range $(M, M + dM)$. It can be normalized to include the fraction of DM in PBHs

$$f_{\text{PBH}} \equiv \frac{\Omega_{\text{PBH}}}{\Omega_{\text{DM}}} = \int dM \psi(M), \quad (3.38)$$

where Ω_{PBH} and Ω_{DM} are the PBH and DM densities in units of critical density.

²Certain aspects of this discussion are largely influenced by [56].

1. **Lognormal Mass Function:** The lognormal model is a good approximation if PBHs result from a smooth symmetric peak in the inflationary power spectrum. [56] It is generally described by

$$\psi(M) = \frac{f_{\text{PBH}}}{\sqrt{2\pi}\sigma M} \exp\left(-\frac{\log^2(M/M_c)}{2\sigma^2}\right), \quad (3.39)$$

where M_c is the mass at which the function $M\psi(M)$ peaks and σ is the width of the spectrum. This model was shown to be disfavoured at the 5% level [57].

2. **Critical Collapse Mass Function:** This model can be generically used if PBHs form from density fluctuations with a δ -function power spectrum.

$$\psi(M) \propto M^{2.85} \exp\left(-\left(M/M_f\right)^{2.85}\right) \quad (3.40)$$

In inflationary scenarios, this expression may be better suited if expressed with two parameters, to simulate a more realistic critical collapse scenario. Further, this model may not be relevant in the case of cosmic strings or matter-dominated ($w = 0$) scenarios.

3. **Multi-Modal PBH Mass Spectrum:** While the three mass models that we have discussed so far give us an idea of the PBH spectrum, they do not portray the entire picture accurately. The mass function should be more complicated than these expressions simply because there could be distinct peaks in the PBH spectrum, depending on the inflaton potential. In [21], the authors describe a multi-modal PBH mass spectrum. They assume that the amplitude of the primordial curvature fluctuations is approximately scale-invariant. This leads to a PBH mass spectrum that peaks at 10^{-6} , 1, 30 and, $10^6 M_\odot$. One of their main predictions include PBH detections in both the lower and upper mass gap regions. This is of particular interest, in our case, since we require PBBH-specific models in the mass gap region for a more detailed answer.

Models Based on Other Parameters

1. **Spin:** Besides mass, the spin parameter is also a salient feature of black holes of all kinds. It possibly carries the footprint of the BH formation mechanism. This riveting fact is directly related to the question we have. If by introducing spin models, we can trace back to the formation mechanism, it would easily help us distinguish between ABBHs and PBBHs. Large spin values generally imply smaller orbital separation at merger, longer inspiral phases and hence, larger integrated fluxes of GWs. [58] With LIGO/Virgo, it is possible to measure the spin of the merger remnant and also the effective spin χ_{eff} of the binary that is given by:

$$\chi_{\text{eff}} = \frac{\vec{J}_1/M_1 + \vec{J}_2/M_2}{M_1 + M_2} \cdot \hat{L}, \quad (3.41)$$

where M_1 and M_2 are the component BH masses, \vec{J}_1 and \vec{J}_2 are the corresponding angular-momentum vectors, and \hat{L} is the direction of the orbital angular momentum.

For the majority of events that we have detected so far, the effective spin parameter is close to zero, with a few exceptions of high-mass events. Implicitly, this means that the χ_{eff} parameter grows with mass. So far, there is no firm prediction for the spin distribution of astrophysical populations. There are two main models that address this - formation of ABBHs in a shared envelope evolution within galactic fields (χ_{eff} and \vec{J} are aligned³) [60]; ABBHs that originated in globular or stellar clusters by dynamical capture in the proximity of active galactic nuclei (spin distribution is approximately zero);

On the other hand, PBHs are generally expected to have formed with nearly-zero spins during the radiation-dominated era. If we were to consider the idea that all the detections so far have been PBBHs [24], this would be an important factor to consider in support of that claim. However, PBHs could be subjected to different conditions as they travel through the universe - gas accretion onto PBHs and the possibility of PBHs merging with each other could both contribute a non-zero spin value.

In [58], the authors describe two spin models as a function of mass and redshift. They focus on the direct dependence of redshift on the accretion rate of PBHs. The main difference between the two models is the assumption of rate of mass accretion before and after redshift $z \sim 10$. They finally conclude that the PBHs with masses below $\mathcal{O}(30)M_{\odot}$ are likely to be non-spinning at any redshift.

2. **Redshift:** We have already discussed a little about the redshift dependence on the accretion rate of PBHs. Further, we need to also consider the dependence of redshift on the merger rate of PBHs. If we consider the distribution of PBH merger rates as functions of redshift z and total mass M , we see that the astrophysical and primordial distributions match very closely at low redshift. But this radically changes at higher redshift $z \geq 1.5$ when the astrophysical rate drops but the primordial rate continues to grow steadily. (Fig. 3.8)
3. **Mass Ratio:** The distribution of mass ratio q values shows a clearer difference between the two populations as astrophysical scenarios tend to favour higher q values. [57]
4. **Orbit Eccentricity:** Eccentricity of the orbit of the binary has the potential to discriminate PBBHs from ABBHs. [8] Circular and eccentric binaries emit GWs that have different waveforms, as seen in Fig. 3.9. This figure shows the direct relation between the eccentricity and the time dependence of the waveform so in principle, it is possible to calculate the initial eccentricity of these objects. Generally, binaries with larger

³some models predict spin misalignment [59]

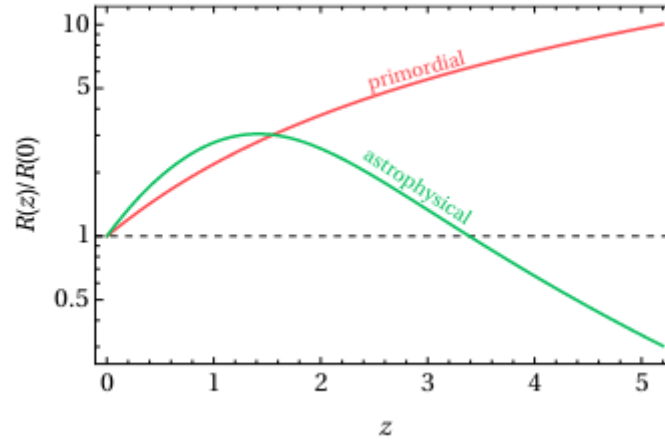


Figure 3.8: **Black Hole Merger Rates**, as a function of redshift; [58]

separation (PBBHs) have smaller eccentricities in the final inspiral phase than those with initial shorter separation (ABBHs). The eccentricity distribution for the LIGO frequency band is expected to have a sharp spike at $e = 0$ for PBHs that formed in the radiation-dominated era.

The future space-based gravitational-wave detector LISA will be sensitive enough to observe the inspiral phase of compact mergers. Thus, it can be used to better detect the eccentricity of the low-frequency compact object orbits during this phase. This topic of study has not been looked into detail yet but might be a good step towards differentiating the two different populations.

3.5.2 Differentiating between ABBH, PBBH and BNS Mergers

Most neutron stars fall within the mass range of 1 to 2 M_{\odot} but there have been studies to show that they could also exist at heavier masses ($> 2M_{\odot}$). In this study, we considered the lower mass gap being populated by light ABBHs and PBBHs but this region might also be populated by heavy BNS mergers. To make it more conclusive, it would be interesting to instead answer the question - *How do we differentiate between stellar binary black holes, primordial binary black holes and binary neutron stars in the lower mass gap?*

One of the first things we have to do while attempting to answer this new question is include a BNS model at higher masses in an approximate range of 2 to 3 M_{\odot} . This also means that we will have to choose which parameter(s) to base the analysis on. A good starting point, similar to our current work, would be to focus on the mass parameters. Once we do this, the rest

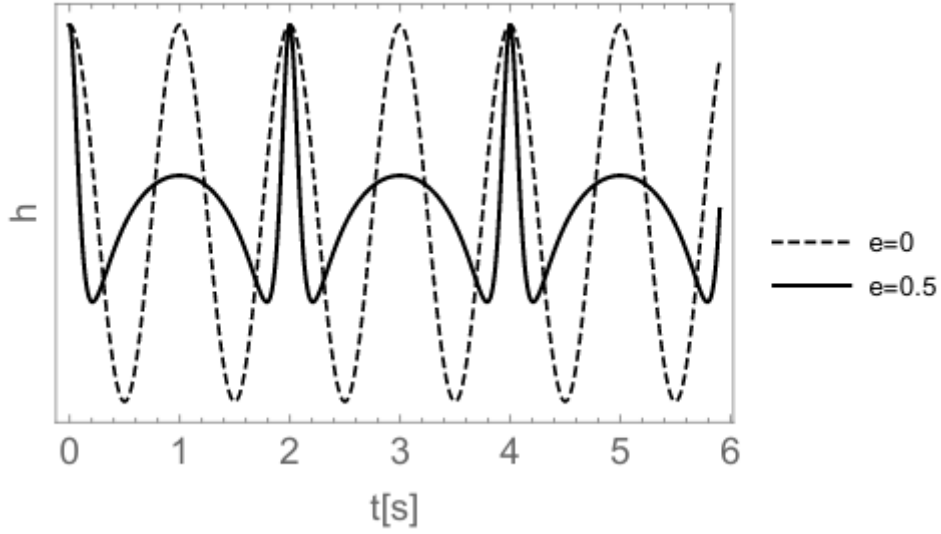


Figure 3.9: **Gravitational waveforms from BH-BH mergers with equal masses of $30 M_{\odot}$** ; The circular orbit ($e = 0$) and the eccentric orbit ($e = 0.5$) clearly have different forms. Amplitude of the waveforms are normalized appropriately. [8]

of the analysis should be as simple as generating new sets of injections for each population and computing the Bayes factor for the different scenarios again. The only caveat is that an analysis of this nature would take several months to finish. Our current analysis took approximately 2-3 months and once we include more low-mass populations, it would take much longer.

The authors in [61] conducted a similar Bayesian analysis between two neutron star mass distribution models. They considered two different scenarios based on m_{max} : in the first scenario, a sharp cut-off was fixed at $m_{max} = 2.9 M_{\odot}$ and in the other, it was taken to be a free parameter as $m_{max} < 2.9 M_{\odot}$. After computing the Bayes factor, the ranges were determined as $2.0 M_{\odot} < m_{max} < 2.2 M_{\odot}$ (68%) and $2.0 M_{\odot} < m_{max} < 2.6 M_{\odot}$ (90%) for either model. In this case, the model selection occurs between the two neutron star mass models. If we were to perform a similar analysis, model selection would take place between mass models of BNS, PBBH and ABBHs.

3.5.3 Case Studies of GW190425 and GW190814

As previously discussed, the recent O3b run detected two events in the lower mass gap region. It would be intriguing to analyze these events particularly and focus on the exotic PBH scenario that both discovery papers mention. [50][51] Many of the detected parameters point towards a primordial black hole detection which makes this an interesting topic to study. The basic distinguishing parameters that we have discussed above are summarized in the table below:

Comparison between GW190425 and GW190814		
Parameter	GW190425	GW190814
Primary Mass (m_1)	1.61 - 2.52 M_\odot	22.2 - 24.3 M_\odot
Secondary Mass (m_2)	1.12 - 1.68 M_\odot	2.5 - 2.67 M_\odot
Mass Ratio (q)	0.4 - 1.0	0.1 - 0.12
Effective Spin (χ_{eff})	0.01 - 0.17	0.059 - 0.062
Redshift (z)	0.01 - 0.04	0.04 - 0.06

3.5.4 Extending to the Upper Mass Gap Region

The LIGO/Virgo detectors are sensitive to detect events with masses up to 100 M_\odot , however, we do not detect anything beyond 50 M_\odot which leads to the region being dubbed as the upper mass gap region. With lower masses, the waveforms become longer which consequently means that we require more time and computational power. If we were to instead analyze the upper mass gap region (>50 M_\odot), it would become easier. The only change that we would need to do is consider different models, and specifically astrophysical and primordial population models that account for the upper mass gap.

ABBHs in the Upper Mass Gap Region

A two-parameter power-law mass distribution, with M_{max} as the free parameter, can be considered

$$p(m_1, m_2 \mid \alpha, M_{\text{max}}) \propto \frac{m_1^{-\alpha} \mathcal{H}(M_{\text{max}} - m_1)}{\min(m_1, M_{\text{tot, max}} - m_1) - M_{\text{min}}}, \quad (3.42)$$

where \mathcal{H} is a Heaviside step function that enforces a cutoff in the distribution at $m_1 = M_{\text{max}}$. [62] The value of α is varied for three simulated AB BH population models with different

values for M_{max} : $M_{max} = 50M_{\odot}$ ($\alpha = 2.35$), $M_{max} = 50M_{\odot}$ ($\alpha = 1$) and, $M_{max} = 40M_{\odot}$ ($\alpha = 2.35$). The first four detections during LIGO's O1 and O2 runs provides evidence towards the last model with a cut-off at $M_{max} \sim 40M_{\odot}$. Hence, this could be considered as the lower boundary value of the upper mass gap. On the other hand, the upper boundary value of the upper mass gap region still remains debatable and largely unknown.

PBBHs in the Upper Mass Gap Region

There are very few studies probing the existence of PBHs in the upper mass gap, and almost no model distributions have been discussed so far. In [21], the authors develop a multi-modal PBH spectrum model that appears to have a peak in the upper mass gap region. This peak refers to the "pion" plateau at around $50 M_{\odot}$. While the approach to the problem is very different in this paper, this information is still very valuable to us when trying to model the upper mass gap region for PBBHs.

Bibliography

- [1] Albert Einstein. “Die grundlage der allgemeinen relativitatstheorie. Annalen der Physik”. In: (1916).
- [2] Eric Thrane and Colm Talbot. “An introduction to Bayesian inference in gravitational-wave astronomy: Parameter estimation, model selection, and hierarchical models”. In: *Publications of the Astronomical Society of Australia* 36 (2019). ISSN: 1448-6083. DOI: [10 . 1017 / pasa . 2019 . 2](https://doi.org/10.1017/pasa.2019.2). URL: [http : / / dx . doi . org / 10 . 1017 / pasa . 2019 . 2](http://dx.doi.org/10.1017/pasa.2019.2).
- [3] B. P. Abbott et al. “Observation of Gravitational Waves from a Binary Black Hole Merger”. In: *Phys. Rev. Lett.* 116 (6 Feb. 2016), p. 061102. DOI: [10 . 1103 / PhysRevLett . 116 . 061102](https://doi.org/10.1103/PhysRevLett.116.061102). URL: [https : / / link . aps . org / doi / 10 . 1103 / PhysRevLett . 116 . 061102](https://link.aps.org/doi/10.1103/PhysRevLett.116.061102).
- [4] B. J. Carr. *Primordial Black Holes - Recent Developments*. 2005. arXiv: [astro - ph / 0504034](https://arxiv.org/abs/astro-ph/0504034) [[astro-ph](https://arxiv.org/abs/astro-ph/0504034)].
- [5] Ya. B. Zel’dovich and I. D. Novikov. “The Hypothesis of Cores Retarded during Expansion and the Hot Cosmological Model”. In: 10 (Feb. 1967), p. 602.
- [6] Stephen Hawking. “Gravitationally collapsed objects of very low mass”. In: 152 (Jan. 1971), p. 75. DOI: [10 . 1093 / mnras / 152 . 1 . 75](https://doi.org/10.1093/mnras/152.1.75).
- [7] B. J. Carr. “The primordial black hole mass spectrum.” In: 201 (Oct. 1975), pp. 1–19. DOI: [10 . 1086 / 153853](https://doi.org/10.1086/153853).

-
- [8] Misao Sasaki et al. “Primordial black holes—perspectives in gravitational wave astronomy”. In: *Classical and Quantum Gravity* 35.6 (Feb. 2018), p. 063001. ISSN: 1361-6382. DOI: [10.1088/1361-6382/aaa7b4](https://doi.org/10.1088/1361-6382/aaa7b4). URL: <http://dx.doi.org/10.1088/1361-6382/aaa7b4>.
- [9] V.F. Mukhanov, H.A. Feldman, and R.H. Brandenberger. “Theory of cosmological perturbations”. In: *Physics Reports* 215.5 (1992), pp. 203–333. ISSN: 0370-1573. DOI: [https://doi.org/10.1016/0370-1573\(92\)90044-Z](https://doi.org/10.1016/0370-1573(92)90044-Z). URL: <http://www.sciencedirect.com/science/article/pii/037015739290044Z>.
- [10] Daniel Baumann et al. “Gravitational wave spectrum induced by primordial scalar perturbations”. In: *Physical Review D* 76.8 (Oct. 2007). ISSN: 1550-2368. DOI: [10.1103/PhysRevD.76.084019](https://doi.org/10.1103/PhysRevD.76.084019). URL: <http://dx.doi.org/10.1103/PhysRevD.76.084019>.
- [11] Kishore N. Ananda, Chris Clarkson, and David Wands. “Cosmological gravitational wave background from primordial density perturbations”. In: *Physical Review D* 75.12 (June 2007). ISSN: 1550-2368. DOI: [10.1103/PhysRevD.75.123518](https://doi.org/10.1103/PhysRevD.75.123518). URL: <http://dx.doi.org/10.1103/PhysRevD.75.123518>.
- [12] Chao Chen and Yi-Fu Cai. “Primordial black holes from sound speed resonance in the inflaton-curvaton mixed scenario”. In: *Journal of Cosmology and Astroparticle Physics* 2019.10 (Oct. 2019), pp. 068–068. ISSN: 1475-7516. DOI: [10.1088/1475-7516/2019/10/068](https://doi.org/10.1088/1475-7516/2019/10/068). URL: <http://dx.doi.org/10.1088/1475-7516/2019/10/068>.
- [13] Yi-Fu Cai et al. “Primordial Black Holes from Sound Speed Resonance during Inflation”. In: *Physical Review Letters* 121.8 (Aug. 2018). ISSN: 1079-7114. DOI: [10.1103/PhysRevLett.121.081306](https://doi.org/10.1103/PhysRevLett.121.081306). URL: <http://dx.doi.org/10.1103/PhysRevLett.121.081306>.
- [14] Yi-Fu Cai et al. “When primordial black holes from sound speed resonance meet a stochastic background of gravitational waves”. In: *Physical Review D* 100.4 (Aug. 2019). ISSN: 2470-0029. DOI: [10.1103/PhysRevD.100.043518](https://doi.org/10.1103/PhysRevD.100.043518). URL: <http://dx.doi.org/10.1103/PhysRevD.100.043518>.
- [15] M.Yu. Khlopov et al. “First-order phase transitions as a source of black holes in the early universe”. In: *Grav. Cosmol.* 6 (2000), pp. 153–156.
- [16] S. W. Hawking, I. G. Moss, and J. M. Stewart. “Bubble collisions in the very early universe”. In: *Phys. Rev. D* 26 (10 Nov. 1982), pp. 2681–2693. DOI: [10.1103/PhysRevD.26.2681](https://doi.org/10.1103/PhysRevD.26.2681). URL: <https://link.aps.org/doi/10.1103/PhysRevD.26.2681>.
- [17] Alexander Polnarev and Robert Zembowicz. “Formation of primordial black holes by cosmic strings”. In: *Phys. Rev. D* 43 (4 Feb. 1991), pp. 1106–1109. DOI: [10.1103/PhysRevD.43.1106](https://doi.org/10.1103/PhysRevD.43.1106). URL: <https://link.aps.org/doi/10.1103/PhysRevD.43.1106>.

- [18] Matthew Lake, Steve Thomas, and John Ward. “String necklaces and primordial black holes from type IIB strings”. In: *Journal of High Energy Physics* 2009.12 (Dec. 2009), pp. 033–033. DOI: [10.1088/1126-6708/2009/12/033](https://doi.org/10.1088/1126-6708/2009/12/033). URL: <https://doi.org/10.1088%2F1126-6708%2F2009%2F12%2F033>.
- [19] Heling Deng, Jaume Garriga, and Alexander Vilenkin. “Primordial black hole and worm-hole formation by domain walls”. In: *Journal of Cosmology and Astroparticle Physics* 2017.04 (Apr. 2017), pp. 050–050. ISSN: 1475-7516. DOI: [10.1088/1475-7516/2017/04/050](https://dx.doi.org/10.1088/1475-7516/2017/04/050). URL: <http://dx.doi.org/10.1088/1475-7516/2017/04/050>.
- [20] Bernard Carr and Florian Kühnel. “Primordial black holes with multimodal mass spectra”. In: *Phys. Rev. D* 99 (10 May 2019), p. 103535. DOI: [10.1103/PhysRevD.99.103535](https://link.aps.org/doi/10.1103/PhysRevD.99.103535). URL: <https://link.aps.org/doi/10.1103/PhysRevD.99.103535>.
- [21] Bernard Carr et al. *Cosmic Conundra Explained by Thermal History and Primordial Black Holes*. 2019. arXiv: [1906.08217](https://arxiv.org/abs/1906.08217) [[astro-ph.CO](https://arxiv.org/archive/astro-ph)].
- [22] Gerald D. Quinlan and Stuart L. Shapiro. “Dynamical Evolution of Dense Clusters of Compact Stars”. In: 343 (Aug. 1989), p. 725. DOI: [10.1086/167745](https://doi.org/10.1086/167745).
- [23] P. C. Peters. “Gravitational Radiation and the Motion of Two Point Masses”. In: *Physical Review* 136.4B (Nov. 1964), pp. 1224–1232. DOI: [10.1103/PhysRev.136.B1224](https://doi.org/10.1103/PhysRev.136.B1224).
- [24] Simeon Bird et al. “Did LIGO Detect Dark Matter?” In: *Physical Review Letters* 116.20 (May 2016). ISSN: 1079-7114. DOI: [10.1103/physrevlett.116.201301](https://doi.org/10.1103/physrevlett.116.201301). URL: <http://dx.doi.org/10.1103/PhysRevLett.116.201301>.
- [25] Misao Sasaki et al. “Primordial Black Hole Scenario for the Gravitational-Wave Event GW150914”. In: *Physical Review Letters* 117.6 (Aug. 2016). ISSN: 1079-7114. DOI: [10.1103/physrevlett.117.061101](https://doi.org/10.1103/physrevlett.117.061101). URL: <http://dx.doi.org/10.1103/PhysRevLett.117.061101>.
- [26] Benjamin V. Lehmann, Stefano Profumo, and Jackson Yant. *Model-independent discovery prospects for primordial black holes at LIGO*. 2020. arXiv: [2007.00021](https://arxiv.org/abs/2007.00021) [[astro-ph.CO](https://arxiv.org/archive/astro-ph)].
- [27] S. Chandrasekhar. “The Maximum Mass of Ideal White Dwarfs”. In: 74 (July 1931), p. 81. DOI: [10.1086/143324](https://doi.org/10.1086/143324).
- [28] Jeremy Tinker et al. “Toward a Halo Mass Function for Precision Cosmology: The Limits of Universality”. In: *The Astrophysical Journal* 688.2 (Dec. 2008), pp. 709–728. ISSN: 1538-4357. DOI: [10.1086/591439](https://doi.org/10.1086/591439). URL: <http://dx.doi.org/10.1086/591439>.
- [29] A. Jenkins et al. “The mass function of dark matter haloes”. In: *Monthly Notices of the Royal Astronomical Society* 321.2 (Feb. 2001), pp. 372–384. ISSN: 1365-2966. DOI: [10.1046/j.1365-8711.2001.04029.x](https://doi.org/10.1046/j.1365-8711.2001.04029.x). URL: <http://dx.doi.org/10.1046/j.1365-8711.2001.04029.x>.

-
- [30] Don N. Page. “Particle emission rates from a black hole: Massless particles from an uncharged, nonrotating hole”. In: *Phys. Rev. D* 13 (2 Jan. 1976), pp. 198–206. DOI: [10.1103/PhysRevD.13.198](https://doi.org/10.1103/PhysRevD.13.198). URL: <https://link.aps.org/doi/10.1103/PhysRevD.13.198>.
 - [31] P. Meszaros. “Primeval black holes and galaxy formation.” In: 38.1 (Jan. 1975), pp. 5–13.
 - [32] B. J. Carr, J. H. Gilbert, and James E. Lidsey. “Black hole relics and inflation: Limits on blue perturbation spectra”. In: *Physical Review D* 50.8 (Oct. 1994), pp. 4853–4867. ISSN: 0556-2821. DOI: [10.1103/physrevd.50.4853](https://doi.org/10.1103/physrevd.50.4853). URL: <http://dx.doi.org/10.1103/PhysRevD.50.4853>.
 - [33] Bernard Carr et al. *Constraints on Primordial Black Holes*. 2020. arXiv: [2002.12778](https://arxiv.org/abs/2002.12778) [[astro-ph.CO](https://arxiv.org/archive/astro-ph)].
 - [34] B. P. Abbott et al. “GW170814: A Three-Detector Observation of Gravitational Waves from a Binary Black Hole Coalescence”. In: *Physical Review Letters* 119.14 (Oct. 2017). ISSN: 1079-7114. DOI: [10.1103/physrevlett.119.141101](https://doi.org/10.1103/physrevlett.119.141101). URL: <http://dx.doi.org/10.1103/PhysRevLett.119.141101>.
 - [35] Sébastien Clesse and Juan García-Bellido. “The clustering of massive Primordial Black Holes as Dark Matter: Measuring their mass distribution with advanced LIGO”. In: *Physics of the Dark Universe* 15 (Mar. 2017), pp. 142–147. ISSN: 2212-6864. DOI: [10.1016/j.dark.2016.10.002](https://doi.org/10.1016/j.dark.2016.10.002). URL: <http://dx.doi.org/10.1016/j.dark.2016.10.002>.
 - [36] Sebastien Clesse and Juan García-Bellido. *Seven Hints for Primordial Black Hole Dark Matter*. 2017. arXiv: [1711.10458](https://arxiv.org/abs/1711.10458) [[astro-ph.CO](https://arxiv.org/archive/astro-ph)].
 - [37] Karsten Jedamzik. *Primordial Black Hole Dark Matter and the LIGO/Virgo observations*. 2020. arXiv: [2006.11172](https://arxiv.org/abs/2006.11172) [[astro-ph.CO](https://arxiv.org/archive/astro-ph)].
 - [38] V. De Luca et al. “Primordial black holes confront LIGO/Virgo data: current situation”. In: *Journal of Cosmology and Astroparticle Physics* 2020.06 (June 2020), pp. 044–044. ISSN: 1475-7516. DOI: [10.1088/1475-7516/2020/06/044](https://doi.org/10.1088/1475-7516/2020/06/044). URL: <http://dx.doi.org/10.1088/1475-7516/2020/06/044>.
 - [39] Benjamin J. Owen and B. S. Sathyaprakash. “Matched filtering of gravitational waves from inspiraling compact binaries: Computational cost and template placement”. In: *Physical Review D* 60.2 (June 1999). ISSN: 1089-4918. DOI: [10.1103/physrevd.60.022002](https://doi.org/10.1103/physrevd.60.022002). URL: <http://dx.doi.org/10.1103/PhysRevD.60.022002>.
 - [40] Kipp Cannon et al. “Singular value decomposition applied to compact binary coalescence gravitational-wave signals”. In: *Physical Review D* 82.4 (Aug. 2010). ISSN: 1550-2368. DOI: [10.1103/physrevd.82.044025](https://doi.org/10.1103/physrevd.82.044025). URL: <http://dx.doi.org/10.1103/PhysRevD.82.044025>.

- [41] Sumeet Kulkarni et al. “Random projections in gravitational wave searches of compact binaries”. In: *Physical Review D* 99.10 (May 2019). ISSN: 2470-0029. DOI: [10 . 1103 / physrevd. 99. 101503](https://doi.org/10.1103/PhysRevD.99.101503). URL: <http://dx.doi.org/10.1103/PhysRevD.99.101503>.
- [42] *Extensions of Lipschitz mappings into a Hilbert space*. Vol. 26. Contemp. Math. Amer. Math. Soc., Providence, RI, 1984, 1982.
- [43] Nick Lord. “Matrix computations, 3rd edition, by G. H. Golub and C. F. Van Loan. Pp. 694. 1996. £25 (paper), £54 (hard). ISBN 0 8018 5414 8, 0 8018 5413 X. (Johns Hopkins University Press).” In: *The Mathematical Gazette* 83.498 (1999), pp. 556–557. DOI: [10 . 2307/3621013](https://doi.org/10.2307/3621013).
- [44] B. P. Abbott et al. “Search for Subsolar-Mass Ultracompact Binaries in Advanced LIGO’s First Observing Run”. In: *Physical Review Letters* 121.23 (Dec. 2018). ISSN: 1079-7114. DOI: [10 . 1103/physrevlett. 121. 231103](https://doi.org/10.1103/physrevlett.121.231103). URL: <http://dx.doi.org/10.1103/PhysRevLett.121.231103>.
- [45] B. P. Abbott et al. “Search for Subsolar Mass Ultracompact Binaries in Advanced LIGO’s Second Observing Run”. In: *Physical Review Letters* 123.16 (Oct. 2019). ISSN: 1079-7114. DOI: [10 . 1103/physrevlett. 123. 161102](https://doi.org/10.1103/physrevlett.123.161102). URL: <http://dx.doi.org/10.1103/PhysRevLett.123.161102>.
- [46] Ryan Magee et al. “Methods for the detection of gravitational waves from subsolar mass ultracompact binaries”. In: *Physical Review D* 98.10 (Nov. 2018). ISSN: 2470-0029. DOI: [10 . 1103/physrevd. 98. 103024](https://doi.org/10.1103/physrevd.98.103024). URL: <http://dx.doi.org/10.1103/PhysRevD.98.103024>.
- [47] Zu-Cheng Chen and Qing-Guo Huang. *Distinguishing Primordial Black Holes from Astrophysical Black Holes by Einstein Telescope and Cosmic Explorer*. 2019. arXiv: [1904 . 02396](https://arxiv.org/abs/1904.02396) [[astro-ph.CO](https://arxiv.org/abs/1904.02396)].
- [48] Antonios Tsokaros et al. “Great Impostors: Extremely Compact, Merging Binary Neutron Stars in the Mass Gap Posing as Binary Black Holes”. In: *Physical Review Letters* 124.7 (Feb. 2020). ISSN: 1079-7114. DOI: [10 . 1103/physrevlett. 124. 071101](https://doi.org/10.1103/physrevlett.124.071101). URL: <http://dx.doi.org/10.1103/PhysRevLett.124.071101>.
- [49] Anuradha Gupta et al. “Black holes in the low-mass gap: Implications for gravitational-wave observations”. In: *Physical Review D* 101.10 (May 2020). ISSN: 2470-0029. DOI: [10 . 1103/physrevd. 101. 103036](https://doi.org/10.1103/physrevd.101.103036). URL: <http://dx.doi.org/10.1103/PhysRevD.101.103036>.
- [50] B. P. Abbott et al. “GW190425: Observation of a Compact Binary Coalescence with Total Mass $3.4 M_{\odot}$ ”. In: *The Astrophysical Journal* 892.1 (Mar. 2020), p. L3. ISSN: 2041-8213. DOI: [10 . 3847/2041-8213/ab75f5](https://doi.org/10.3847/2041-8213/ab75f5). URL: <http://dx.doi.org/10.3847/2041-8213/ab75f5>.

-
- [51] R. Abbott et al. “GW190814: Gravitational Waves from the Coalescence of a 23 Solar Mass Black Hole with a 2.6 Solar Mass Compact Object”. In: *The Astrophysical Journal* 896.2 (June 2020), p. L44. DOI: [10.3847/2041-8213/ab960f](https://doi.org/10.3847/2041-8213/ab960f). URL: <https://doi.org/10.3847/2041-8213/ab960f>.
 - [52] J. Veitch et al. “Parameter estimation for compact binaries with ground-based gravitational-wave observations using the LALInference software library”. In: *Phys. Rev. D* 91 (4 Feb. 2015), p. 042003. DOI: [10.1103/PhysRevD.91.042003](https://link.aps.org/doi/10.1103/PhysRevD.91.042003). URL: <https://link.aps.org/doi/10.1103/PhysRevD.91.042003>.
 - [53] Gregory Ashton et al. “Bilby: A User-friendly Bayesian Inference Library for Gravitational-wave Astronomy”. In: *The Astrophysical Journal Supplement Series* 241.2 (Apr. 2019), p. 27. ISSN: 1538-4365. DOI: [10.3847/1538-4365/ab06fc](http://dx.doi.org/10.3847/1538-4365/ab06fc). URL: <http://dx.doi.org/10.3847/1538-4365/ab06fc>.
 - [54] B. P. Abbott et al. “Binary Black Hole Mergers in the First Advanced LIGO Observing Run”. In: *Phys. Rev. X* 6 (4 Oct. 2016), p. 041015. DOI: [10.1103/PhysRevX.6.041015](https://link.aps.org/doi/10.1103/PhysRevX.6.041015). URL: <https://link.aps.org/doi/10.1103/PhysRevX.6.041015>.
 - [55] B. P. Abbott et al. “Binary Black Hole Population Properties Inferred from the First and Second Observing Runs of Advanced LIGO and Advanced Virgo”. In: *The Astrophysical Journal* 882.2 (Sept. 2019), p. L24. ISSN: 2041-8213. DOI: [10.3847/2041-8213/ab3800](http://dx.doi.org/10.3847/2041-8213/ab3800). URL: <http://dx.doi.org/10.3847/2041-8213/ab3800>.
 - [56] Bernard Carr et al. “Primordial black hole constraints for extended mass functions”. In: *Physical Review D* 96.2 (July 2017). ISSN: 2470-0029. DOI: [10.1103/physrevd.96.023514](http://dx.doi.org/10.1103/PhysRevD.96.023514). URL: <http://dx.doi.org/10.1103/PhysRevD.96.023514>.
 - [57] Andrew D. Gow et al. “Primordial black hole merger rates: distributions for multiple LIGO observables”. In: *Journal of Cosmology and Astroparticle Physics* 2020.01 (Jan. 2020), pp. 031–031. ISSN: 1475-7516. DOI: [10.1088/1475-7516/2020/01/031](http://dx.doi.org/10.1088/1475-7516/2020/01/031). URL: <http://dx.doi.org/10.1088/1475-7516/2020/01/031>.
 - [58] V. De Luca et al. “The evolution of primordial black holes and their final observable spins”. In: *Journal of Cosmology and Astroparticle Physics* 2020.04 (Apr. 2020), pp. 052–052. ISSN: 1475-7516. DOI: [10.1088/1475-7516/2020/04/052](http://dx.doi.org/10.1088/1475-7516/2020/04/052). URL: <http://dx.doi.org/10.1088/1475-7516/2020/04/052>.
 - [59] Davide Gerosa et al. “Resonant-plane locking and spin alignment in stellar-mass black-hole binaries: A diagnostic of compact-binary formation”. In: *Physical Review D* 87.10 (May 2013). ISSN: 1550-2368. DOI: [10.1103/physrevd.87.104028](http://dx.doi.org/10.1103/PhysRevD.87.104028). URL: <http://dx.doi.org/10.1103/PhysRevD.87.104028>.
 - [60] Luc Blanchet. “Gravitational Radiation from Post-Newtonian Sources and Inspiralling Compact Binaries”. In: *Living Reviews in Relativity* 17.1 (Feb. 2014). ISSN: 1433-8351. DOI: [10.12942/lrr-2014-2](http://dx.doi.org/10.12942/lrr-2014-2). URL: <http://dx.doi.org/10.12942/lrr-2014-2>.

- [61] Justin Alsing, Hector O Silva, and Emanuele Berti. “Evidence for a maximum mass cut-off in the neutron star mass distribution and constraints on the equation of state”. In: *Monthly Notices of the Royal Astronomical Society* 478.1 (Apr. 2018), pp. 1377–1391. ISSN: 1365-2966. DOI: [10.1093/mnras/sty1065](https://doi.org/10.1093/mnras/sty1065). URL: <http://dx.doi.org/10.1093/mnras/sty1065>.
- [62] Maya Fishbach and Daniel E. Holz. “Where Are LIGO’s Big Black Holes?” In: 851.2, L25 (Dec. 2017), p. L25. DOI: [10.3847/2041-8213/aa9bf6](https://doi.org/10.3847/2041-8213/aa9bf6). arXiv: [1709.08584](https://arxiv.org/abs/1709.08584) [[astro-ph.HE](#)].